frontiers

Mechanics of Crater-Enabled Soft Dry Adhesives: A Review

Liu Wang[1], Kyoung-Ho Ha[1], Gregory J. Rodin[1], Kenneth M. Liechti[1], Nanshu Lu[1*]

[1]University of Texas at Austin, United States

Submitted to Journal:
Frontiers in Mechanical Engineering

Specialty Section:
Tribology

Article type:
Review Article

Manuscript ID:
601510

Received on:
01 Sep 2020

Revised on:
16 Oct 2020

Frontiers website link:
www.frontiersin.org

Conflict of interest statement

The authors declare that the research was conducted in the absence of any commercial or financial relationships that could be construed as a potential conflict of interest

Author contribution statement

L. Wang, K. Ha, G.J. Rodin, K. Liechti, N. Lu participated fully to the data acquisition, analysis, and paper writing. All authors contributed to the article and approved the submitted version.

Keywords

dry adhesive, Suction, CRaTER, Micro-pillar, Adhesive strength, Underwater Adhesion

Abstract

Word count: 171

Dry adhesion is governed by physical rather than chemical interactions. Those may include van der Waals and electrostatic forces, friction, and suction. Soft dry adhesives (SDAs), which can be repeatedly attached to and detached from surfaces, can be useful for many exciting applications including reversible tapes, robotic footpads and grippers, and bio-integrated electronics. So far, the most studied SDAs are gecko-inspired micro-pillar arrays, but they suffer from limited reusability and weak adhesion underwater. Recently cratered surfaces emerged as an alternative to micro-pillar arrays, as they exhibit many advantageous properties, such as tunable pressure-sensitive adhesion, high underwater adhesive strength, and good reusability. This review summarizes the recent work of the authors on the mechanical characterization of cratered surfaces, which combines experimental, modeling, and computational components. Using fundamental relationships describing air or liquid inside the crater, we examine the effects of material properties, crater shapes, air vs. liquid ambient environments, and surface patterns. We also identify some unresolved issues and limitations of the current approach and provide an outlook for future research directions.

Contribution to the field

After about six years of studies, crater-enabled soft dry adhesives (SDA) are still in its infancy. The mechanics and realization of practically useful cratered SDAs are still elusive with wide-open oppurtunities. Our review offers the fundamental understanding of the underlying mechanism which helps the future exploration of optimal design of SDAs with enhanced properties.

Funding statement

All authors acknowledge the support from the National Science Foundation (NSF) Division of Civil, Mechanical and Manufacturing Innovation (CMMI) award (Grant No. 1663551). Liu Wang acknowledges the Warren A. and Alice L. Meyer endowed graduate fellowship awarded by the Cockrell School of Engineering at the University of Texas at Austin. Kyoung-Ho Ha acknowledges the Philip C. and Linda L. Lewis Foundation Graduate Fellowship in Mechanical Engineering at the University of Texas at Austin.

Mechanics of Crater-Enabled Soft Dry Adhesives: A Review

Liu Wang[1], Kyoung-Ho Ha[2], Gregory J. Rodin[1], Kenneth M. Liechti[1], Nanshu Lu[1,2,3,4]*

[1]*Center for Mechanics of Solids, Structures and Materials,*

Department of Aerospace Engineering and Engineering Mechanics

[2]*Departement of Mechanical Engineering,*

[3]*Department of Biomedical Engineering,* [4]*Texas Materials Institute,*

The University of Texas at Austin, Austin, Texas 78712, United States

Abstract

Dry adhesion is governed by physical rather than chemical interactions. Those may include van der Waals and electrostatic forces, friction, and suction. Soft dry adhesives (SDAs), which can be repeatedly attached to and detached from surfaces, can be useful for many exciting applications including reversible tapes, robotic footpads and grippers, and bio-integrated electronics. So far, the most studied SDAs are gecko-inspired micro-pillar arrays, but they suffer from limited reusability and weak adhesion underwater. Recently cratered surfaces emerged as an alternative to micro-pillar arrays, as they exhibit many advantageous properties, such as tunable pressure-sensitive adhesion, high underwater adhesive strength, and good reusability. This review summarizes recent work of the authors on mechanical characterization of cratered surfaces, which combines experimental, modeling, and computational components. Using fundamental relationships describing air or liquid inside the crater, we examine the effects of material properties, crater shapes, air *vs.* liquid ambient environments, and surface patterns. We also identify some unresolved issues and limitations of the current approach, and provide an outlook for future research directions.

Keywords: dry adhesive, micro-pillar, crater, suction, underwater adhesion, adhesive strength

* Corresponding author: nanshulu@utexas.edu, 512-471-4208, 2617 Wichita Street, C0600, Austin, TX 78712

I. Introduction

Soft adhesives are conformable and deformable binding agents between two surfaces. Engineered soft adhesives have become part of our daily life, *e.g.,* medical bandages for wound healing, stretchable brace tapes for joint protection, and double-sided tapes for paper sticking. Soft adhesives are usually categorized as either soft wet adhesives (SWAs) or soft dry adhesives (SDAs). SWAs bond surfaces together through either chemical reactions or mechanical loading (Czech et al., 2013;Cho et al., 2019;Yuk et al., 2019;Chen et al., 2020a). For example, a well-known ~~type~~ class of SWAs is pressure-sensitive adhesives (PSAs) which consist of a viscoelastic bonding agent that can instantaneously form a bond to the adherend under applied pressure (Creton, 2003;Czech and Kowalczyk, 2011). Acrylics, polyether, silicones, polyesters, and polyurethanes are commonly used bonding agent for PSAs (Singh et al., 2011;Cilurzo et al., 2012). Due to their viscous nature, PSAs can flow to conform to rough surfaces upon compression, and the inherent tackiness and low surface energy of the adhesive materials facilitate strong bonding onto a variety of substrates (Singh et al., 2014). However, with the rapid development of bioelectronics and the increasing demand for seamless integration between humans and machines, conventional SWAs are facing some challenges. First, despite their relatively strong bonding capability, the tacky binding agent can be easily contaminated with impurities (e.g., dust, sebum, etc.), limiting both the ability to reposition and reuse. Second, the binding agent may contain chemicals harmful to humans, resulting in irritation (Kawahara and Tojo, 2007), contact dermatitis (Christoffers et al., 2014), and even injury or damage (Matsumura et al., 2013;Hwang et al., 2018). In contrast, SDAs bond by employing physical interactions such as electrostatic attraction, van der Waals (vdW) forces, suction, or friction (Eisenhaure and Kim, 2017). In general, SDAs require relatively smooth surfaces to enable ~~the~~ such physical interactions, e.g., no air leakage or intimate contact for vdW interaction, thus they were not used as widely as SWAs. But in the last two decades, SDAs have garnered tremendous attention with great promise in the fields of healthcare, soft robotics, and human-machine interface (Brodoceanu et al., 2016;Li et al., 2016;Xiaosong et al., 2019;Chen et al., 2020b). Of particular interest are SDAs that are capable of repeated attachment and detachment, whose usefulness has been demonstrated in many exciting applications such as breathable skin patches (Kwak et al., 2011), robotic footpads or grippers (Gorb et al., 2007), and reusable bio-integrated electronics (Hwang et al., 2018).

II. Pillar- and Crater-Enabled SDAs

So far, the most widely studied SDAs are surfaces with arrays of micro-pillars. The inspiration came from terrestrial species including lizards and geckos whose toe pads are covered by intricate fibrils that enable strong attachment as well as easy release (Autumn et al., 2000;Autumn et al., 2002;Arzt et al., 2003;Gao and Yao, 2004;Hansen and Autumn, 2005;Yao and Gao, 2006). Autumn *et al.* (Autumn et al., 2000) first discovered the hierarchical *lamellae* and *setae* structures of gecko toe pads by scanning electron microscopy (SEM). There, each seta branches into hundreds of 200-nm thin *spatula*, capable of conforming to curvilinear and rough surfaces. The normal adhesive strength of those toe pads was measured at of 100 kPa (Autumn et al., 2000), which is comparable to that of a 3M Scotch^{TM} tape (200 kPa). The strong adhesion of the gecko toe pads was solely attributed to van der Waals (vdW) forces between the nanoscale spatula and the target surface, rather than chemical bonding (Autumn et al., 2002). Aside from the remarkable attachment performance, the fibrillary system also exhibits superior reversibility and self-cleaning capability (Hansen and Autumn, 2005).

Figures 1A-1E showcase several representative synthetic micro-scale surface features resembling gecko fibrils. The simplest design is micro-pillars with flat tips (Del Campo and Arzt, 2007;del Campo et al., 2007a;Del Campo et al., 2007b) (Figure 1A). More advanced designs involve micro-pillars with hierarchy (Greiner et al., 2009;Wang et al., 2014) (Figure 1B). Spatula tips (Del Campo and Arzt, 2007;del Campo et al., 2007a) (Figure 1C) have been designed to more closely mimic the gecko's toe pads. Emulating the design principle of the tilting setae on gecko's toe pads, slanted structures have been widely exploited to generate directional adhesion (Figure 1D) (Autumn et al., 2006a;Murphy et al., 2009;Moon et al., 2010;Afferrante and Carbone, 2012;Jin et al., 2014;Wang et al., 2014;Wang et al., 2015;Seo et al., 2016;Wang, 2018). ~~It~~ This represents a breakthrough in developing reversible adhesives that truly resemble their natural prototypes. Among all the tip geometries, the mushroom-like shape (Figure 1E) stands out as it exhibits large adhesive strength by reducing the stress concentration at the pillar-substrate interfaces (del Campo et al., 2007a;Carbone et al., 2011;Carbone and Pierro, 2012;Bae et al., 2013;Wang et al., 2014;Marvi et al., 2015;Kim et al., 2016). The vibrant research on micro-pillar-based SDAs has been summaried by many excellent review articles, with various focuses on the adhesion mechanisms, design principles, fabrication methods, and performance characterizations

(Pattantyus-Abraham et al., 2013;Zhou et al., 2013;Sahay et al., 2015;Eisenhaure and Kim, 2017;Xiaosong et al., 2019). Figures 1F-1L display examples of another type of SDAs, suction- or crater-based adhesives, which is the focus of this paper and will be discussed in detail later.

Despite extensive research in the last two decades, as far as applications are concerned, micro-pillar-enabled SDAs are facing some major barriers. First, according to "contact splitting" theory (Arzt et al., 2003;Chan et al., 2007;Kamperman et al., 2010), the adhesion can be enhanced by splitting up the contact with the adherend into finer subcontacts, enabled by extremely tiny fibrils. However, scaling-down the pillar size faces fundamental physical limitations and dramatically increases manufacturing difficulties and costs. Those challenges have been recognized in both electron beam lithography (Pease, 1981;Vieu et al., 2000) and nano-embossing (Becker and Heim, 2000;Kim et al., 2007). Furthermore, slender pillars are prone to buckling and collapsing, resulting in undesirable entanglements and/or mats (see Figure 2A). In fact, buckling may even lead to rupture and detachment (Chan et al., 2007;Del Campo and Arzt, 2007;Greiner et al., 2007;Kim et al., 2007;Kim et al., 2016;Eisenhaure and Kim, 2017). All of these degradation mechanisms may significantly impair the adhesive strength, leading to limited robustness and reusability. On a different note, it has been widely reported that micro-pillars may lose their van der Waals adhesion on wet surfaces or in aquatic environments (Buhl et al., 2009;Pesika et al., 2009;Baik et al., 2017;Cadirov et al., 2017;Ma et al., 2018). A typical adhesion test shown in Figure 2B unveils that humidity dramatically decreases the adhesion of micro-pillar arrays (Cadirov et al., 2017). This is consistent with another experimental observation that micro-pillar arrays almost completely lose adhesion with moisture or underwater (see the green bars in Figure 2C) (Baik et al., 2017). Figure 2D, taken from the same paper (Baik et al., 2017), highlights the adhesion of cratered surfaces, which will be discussed later.

According to Bartlett *et al.* (Bartlett et al., 2012;Bartlett and Crosby, 2014), the adhesive force of micro-pillars can be scaled as $F_{ad} \sim \sqrt{A/C}$ where A is the actual contact area and C is the system compliance in the loading direction. Based on this scaling law, aside from enlarging effective contact area A, the adhesive force may also be enhanced by decreasing the system compliance C. An easy way to minimize the compliance C is by utilizing stiff materials. Here, we summarize existing data from the literature in an Ashby plot (Figure 3, numbers are listed in Table 1 and Table 2) where the experimentally measured normal adhesive strength is plotted versus

material Young's modulus (Geim et al., 2003;Sitti and Fearing, 2003;Kim and Sitti, 2006;Del Campo et al., 2007b;Lee et al., 2008;Lu et al., 2008;Cheung and Sitti, 2009;Davies et al., 2009;Murphy et al., 2009;Parness et al., 2009;Sameoto and Menon, 2009;Kwak et al., 2011;Bae et al., 2013;Tsai and Chang, 2013;Jin et al., 2014;Fischer et al., 2016;Kim et al., 2016;Drotlef et al., 2017;Hu et al., 2017). In this plot, the purple zone represents pillar-based adhesives in dry environments, the orange zone highlights crater-based adhesives under normal ambient conditions, and the green zone indicates crater-based adhesives under high humidity, wet or underwater environments. In particular, setae (material: β-keratin with E ~ 1-2GPa) on gecko toe pads can produce ~100 kPa adhesive strength (Autumn et al., 2000;Autumn et al., 2006b;Huber et al., 2008) as highlighted by the gecko icon in the plot. To achieve adhesion on par with gecko toe pads, stiff materials are usually employed such as polythiophene nanotubes (E ~ GPa) (Lu et al., 2008) and carbon nanotubes (E ~ TPa) (Zhao et al., 2006). But reducing the compliance C would also inherently compromise the softness of the adhesive and their conformability to curvilinear surfaces, especially when the surface is deformable (e.g., human skin), (Qiao et al., 2015;Wang and Lu, 2016;Wang et al., 2017a), which limits their applications. However, when micro-pillars are fabricated out of soft materials (E < 3MPa), their adhesive performance is significantly compromised as shown in Figure 3, resulting in two distinctive purple zones.

Another class of reusable SDAs emerged as arrays of micro-craters (i.e., dimples or depressions engineered on polymer surfaces). In fact, utilizing suction for attachment has been widely observed in nature. The arms of aquatic cephalopods such as squid and octopus are equipped with hundreds of suckers for anchoring and object manipulation (Smith, 1991;Kier and Smith, 2002;Von Byern and Klepal, 2006;Tramacere et al., 2013;Tramacere et al., 2014b). The pressure drop inside the sucker, termed negative pressure, can reach 300 kPa for octopus and 800 kPa for decapod (Smith, 1991;Smith, 1996). Cephalopod suckers have been emulated on aquatic robots using active pumps (Wang et al., 2017c;Shintake et al., 2018) as well as passive adhesive tapes (Choi et al., 2016;Baik et al., 2017). Passive cratered surfaces have demonstrated remarkable adhesion capabilities in recent years. Just to name a few, in 2014, Chang *et al.* (Chang et al., 2014) created an array of submicron-sized craters on UV resin (Figure 1G) and measured adhesive shear strengths as high as 750 kPa on silicon wafers (Chang et al., 2014). In 2015, Choi *et al.* fabricated an array of 1-μm-diameter craters on the surface of a multilayer polydimethylsiloxane (PDMS) (Figure 1H) and the measured adhesive strength exceeded that of the same PDMS with either flat

or pillared surface (Choi et al., 2016). Also in 2015, Akerboom *et al.* fabricated close-packed nano-dimples on 10:1 (base-to-curing agent ratio) PDMS (Figure 1I) and found a larger pull-off force in comparison to flat PDMS surfaces (Akerboom et al., 2015). In 2017, Baik *et al.* fabricated dome-shaped protuberances within micro-craters (Figure 1J), whose adhesive strength was found to be 2-3 times higher than micro-pillars in dry condition (Baik et al., 2017). Similarly, enhanced adhesion has been reported by Nanni *et al.* who engineered PDMS with square-shaped craters (Figure 1K) (Nanni et al., 2015).

Beyond simple pillars or craters, researchers have combined the pillar effects with the suction mechanism. It has been experimentally confirmed that suction contributed 20% towards the total adhesive force in mushroom-like micro-pillars (Varenberg and Gorb, 2008;Tinnemann et al., 2019). The authors argued that vacuum may be generated between the thin mushroom-like tip and the surface during the detachment. In fact, micro-pillar stalks terminated with concave dome tip(Baik et al., 2018) (Figure 1F) or funnel-shaped tip (Fischer et al., 2017) (Figure 1L) have been realized and adhesive strength has been elevated to an ultrahigh value of 5.6 MPa (Fischer et al., 2017), which is gigantic compared with kPa-range adhesive strengths for simple pillars (e.g., Figure 1A-1E) or simple craters (Figure 1G-1K).

Although both are SDAs, crater-enabled adhesives have the following advantages ~~in~~ relative to pillar-enabled adhesives: ease of fabrication, pressure-sensitive adhesion, excellent wet adhesion, superior scratch resistance and reusability, and high material compliance. Generally, cratered surfaces are engineered by molding a soft elastomer on a negative template with domes. Such a fabrication method is generally easier than the process to produce hierarchical (Del Campo and Arzt, 2007;Greiner et al., 2009) or composite micro-pillars (Bae et al., 2013;Drotlef et al., 2019). Distinct from the micro-pillars whose adhesive strength is usually fixed once fabricated (Murphy et al., 2009;Mengüç et al., 2012;Chary et al., 2013), the adhesion of cratered surfaces depends on the preload (Akerboom et al., 2015;Baik et al., 2019b). It is also worth noting that crater arrays, similar to octopus suckers, show a conspicuously enhanced adhesive strength underwater or on wet surfaces (see the red bar in Figure 2c and the green domain in Figure 3). Also, without delicate protruding structures, cratered surfaces are more scratch resistant and reusable. For example, Baik *et al.*(Baik et al., 2017) demonstrated that the adhesive force of craters remained almost unchanged after 10000 cycles of attachment and detachment (Figure 2D). Last

but not least, as presented in Figure 3, crater-enabled SDAs are capable of producing higher adhesion while maintaining the desirable levels of material softness. Such high softness endows them with exceptional deformability as well as conformability on deformable, rough surfaces including bio-tissues (Choi et al., 2016). These advantages of crater-based adhesives have enabled many exciting applications including wall-climbing robots (Aksak et al., 2008;Sahay et al., 2015), object manipulation (Chang et al., 2014) such as wafer handling (Lee et al., 2016), and bio-integrated medical devices (Chun et al., 2018;Hwang et al., 2018;Oh et al., 2018;Baik et al., 2019a;Baik et al., 2019c;Kim et al., 2019;Iwasaki et al., 2020).

Let us point out that harnessing suction for attachment is ubiquitous. Thin-walled suction cups are widely used in everyday suction hooks and climbing robot pads (Figure 4A) (Yoshida and Ma, 2010;Manabe et al., 2012) due to their strong attachment and quick release. By assembling suction cups onto a tapered elastomeric arm, Xie *et al.* recently demonstrated a soft actuator that was capable of grasping objects of various shapes (Figure 4B) (Xie et al., 2020). The same group also provided a feasible solution for preventing air leakage when gripping rough surfaces by programming the compliance of the sucker. The sucker was made of electrically responsive organohydrogel, which softened under high voltage, giving rise to conformable contact with rough surfaces (Figure 4C) (Zhuo et al., 2020). Theoretical analysis and experimental measurements have been carried out to understand both the attachment and detachment behaviors of suction cups. For instance, by actively pumping out the air through a connected tube, Liu *et al.*(Liu et al., 2006) has reported the relationship between the negative pressure inside the cup and the active area, i.e. the area not in contact between the cup and the substrate. The suction force can be readily obtained through negative pressure multiplied by the active area. Different from air-pumping, Ge *et al.* proposed a pushing-detaching framework for characterizing the suction force of a commonly used passive suction cup (Figure 4D) (Ge et al., 2015). The process is illustrated in Figure 4D. In the beginning, the cup is resting on the substrate surface. Then a preload is applied to deform the suction cup such that air inside the cup is squeezed out and the suction cup successfully attaches to the substrate. To detach it, a pulling force is applied until it reaches the pull-off force. Based on this process, the suction force of the cup has been modeled and experimentally validated. However, such analysis is only applicable to thin-walled suction cups rather than craters which are dimples on the surface surrounded by the polymer matrix.

Despite a significant body of experimental evidence that suction is a significant adhesion mechanism for cratered surfaces, until recently, theoretical understanding and consequently model-guided design procedures were lacking. Our recent series of ~~work~~ papers were a ~~scarce~~ attempt intended to remedy this situation. We have developed an integrated computational-experimental-modeling approach for the quantitative characterization and understanding of the suction behaviors for various cratered surfaces under both dry and wet conditions. In the next section, we summarize our results by focusing on four factors controlling suction of isolated craters (Figure. 5): Young's modulus of the polymer matrix (Figure 5A) (Qiao et al., 2017), crater shape (Figure 5B) (Qiao et al., 2017;Wang et al., 2019), air/underwater ambient environment (Figure 5C) (Wang et al., 2017b;Qiao et al., 2018), and elasto-capillary effect on micro/nano-craters (Figure 5D) (Wang et al., 2017b). In Section IV, we will discuss cratered surfaces and address the importance of the crater areal fraction as defined by the ratio between the projected area of crater and the base plane area of specimen (Figure 5E) (Wang et al., 2019) and patterns (Figure 5F) (Wang et al., 2019) of cratered arrays.

III. Isolated Craters

This section summarizes our results for isolated craters. The term isolated means that the crater dimensions are much smaller than all other specimen dimensions, and therefore the specimen can be regarded as a semi-infinite solid, where the only relevant dimensions are those of the crater.

3.1. Isolated craters in air

We begin this section by considering isolated craters in air as a precursor to considering the presence of liquids on the performance of isolated craters.

3.1.1. Modeling framework

Following the earlier work on thin-walled suction cups (Ge et al., 2015), a loading-unloading process is established for calculating the suction force of an isolated crater, as illustrated by Figures 6A-6C. Initially, the air inside the crater is characterized by the ambient pressure, p_0,

volume V_0, and number of molecules N_0 (Figure 6A). The suction effect is realized in the following two steps:

1. The specimen is subjected to a remote compressive stress σ, which squeezes air out of the crater. We refer to σ as the preload, and denote the state at the end of this step by the triplet (p_1, V_1, N_1) (Stage 1, Figure 6B).
2. The specimen is unloaded in such a manner that air does not return to the crater and the crater springs back. This action results in a pressure drop inside the crater which produces the suction force. At the end of this step, the air in the crater is characterized by the triplet (p_2, V_2, N_2) (Stage 2, Figure 6C). Accordingly, the pressure drop is

$$-\Delta p = p_1 - p_2$$

and the suction force

$$F = -\Delta p A_2 \tag{1}$$

where A_2 is the projected area of the crater at Stage 2.

Key assumptions adopted in this framework are:

(a) The air flows freely out of the crater upon loading (Step 1), so that $p_1 = p_0$.

(b) No air exchange takes place upon unloading (Step 2), so that $N_2 = N_1$.

(c) The entire process is isothermal and air is an ideal gas, so that $p_1 V_1 = p_2 V_2$.

Assumptions (a) and (b) are consistent with the abovementioned models of thin-walled suction cups (Liu et al., 2006;Ge et al., 2015). However, in our experiment, to be discussed later, Assumption (a) is hard to achieve without a vent hole drilled in the substrate. Therefore, future research is required to realize Assumption (a) without any vent hole. Furthermore, secure sealing after loading should be validated to justify Assumption (b). With these three assumptions, the pressure drop can be related to the crater volumes as

$$-\Delta p = \left(1 - \frac{V_1}{V_2}\right) p_0 \tag{2}$$

Therefore, the suction force becomes

$$F = \left(1 - \frac{V_1}{V_2}\right) p_0 A_2. \quad (3)$$

If the ambient pressure is equal to the atmospheric pressure p_a , we can define the suction-induced effective adhesive strength as

$$\sigma_{eff} = \frac{F}{A_0} = \left(1 - \frac{V_1}{V_2}\right) \frac{A_2}{A_0} p_a. \quad (4)$$

According to this equation, obtaining a large value of σ_{eff} requires both small V_1 after loading, and large A_2 and V_2 after unloading. The maximum possible σ_{eff} is atmospheric pressure, i.e., p_0, which can be achieved when the crater is fully closed after loading, i.e., $V_1 = 0$, and recovers to $A_2 = A_0$ after unloading.

3.1.2. Simulation and experimental setups

Axisymmetric finite element models (FEM) for isolated craters were built to simulate the suction force using commercial software, ABAQUS 6.13 (Figure 6D). The built-in function *FLUID CAVITY was implemented to model the ideal gas behavior inside the craters. The specimen/substrate interface was assumed to be frictionless, and the substrate was assumed to be rigid. The material behavior of 30:1 PDMS was characterized as an incompressible neo-Hookean model with Young's modulus $E = 141.9$ kPa according to our measurements(Qiao et al., 2017). Experimentally, polydimethylsiloxane (PDMS) with base-to-curing-agent mass ratio equal to 30:1 was cured at 70℃ for 12 h to mold specimens with and without craters (see inset in Figure 6E). A small vent hole with diameter of 0.8 mm was drilled in the rigid plate and roughly aligned with the center of the crater. Oil lubricant was applied at the specimen/plate interface. Loading and unloading tests were carried out with the vent hole open during loading and closed during unloading and the pull-off force was measured. A representative experimental loading-unloading curve is given in Figure 6E. The suction force can be readily calculated by subtracting the adhesive force over the contact zone (which is very small and independent of preload) from the measured pull-off force at the pull-off point (Qiao et al., 2017).

3.1.3. Results

Spherical-cap-shaped (SCS) craters with various aspect ratios were studied both numerically and experimentally. The schematic of a SCS crater is shown in Figure 5B where the base radius and height of the craters are labeled as a and b, repectively. Figure 6F plots the effective adhesive strength σ_{eff} as a function of preload for two aspect ratios, $b/a = 1$ (blue) and $b/a = 2/3$ (red). Experimental results are plotted as markers and FEM results as solid curves. The following conclusions can be drawn from Figure 6F. First, suction-enabled adhesion intrinsically depends on preload, and generally higher suction force can be achieved by increasing the preload. Second, when the preload is large enough to fully close the crater at Stage 1, further compression will not enhance the suction anymore as shown by the plateau of the two curves. Third, under small preloads, shallower craters generate higher suction forces than deeper ones.

It is also worth noting that experimental and FEM results agree well. Therefore, such a simulation approach can be confidently used for characterizing other cratered specimens, e.g., of different Young's moduli and crater shapes. A contour plot for the effective adhesive strength as a function of material Young's modulus E and aspect ratio b/a is given in Figure 6G. Results presented in Figure 6G are evaluated at full closure, i.e., $-\Delta p = p_0$ is attained for all scenarios. It is clear that deeper craters with stiffer matrices are capable of producing larger suction provided full closure at Stage 1. Note that it is an opposite conclusion compared with what we discussed in Figure 6F – shallower crater generates higher suction provided the same preload. This can be understood as follows: it is easier for shallower craters to reach full closure when the preload is small, i.e., a smaller V_1, thus achieve a higher suction force according to Eq. (4). However, when the preload is large enough to fully close craters, i.e., $V_1 = 0$, deeper craters will spring back more with a larger projected area, i.e., a large A_2, giving rise to a higher suction force. The black curve in Figure 6G represents an iso-strength curve of $\sigma_{eff} = 80$ kPa. Note that crater shape is limited to a spherical cap in Figure 6G and is varied by choosing different aspect ratios. Other shapes such as spheroidal (Qiao et al., 2017) and cylindrical (Wang et al., 2019) craters have also been investigated but are not discussed in this review.

3.2. Macroscopic, isolated craters underwater

Similar to suction cups on aquatic cephalopods (Tramacere et al., 2014a;Tramacere et al., 2014b), craters underwater also exhibit much larger adhesive strength than those in air (see Figure 3). This is addressed by considering a cratered specimen resting on a fixed rigid platform, both submerged in liquid at depth h (Figure 5C). The ambient pressure is now

$$p_0 = \rho g h + p_a \tag{5}$$

where ρ is the liquid density and g is the gravitational constant. Assume that the suction force is still generated through a loading-unloading process as illustrated in Figure 6A but in an aquatic environment. Similar to air-filled craters, the pressure inside the crater at States 0 and 1 are assumed to be the same, i.e., $p_1 = p_0$ and the number of liquid molecules remains unchanged during State 2, i.e., $N_1 = N_2$. However, rather than adopting the ideal gas relationship $p_1V_1 = p_2V_2$, the liquid inside the crater is assumed to be incompressible, so that $V_1 = V_2$. Both FEM and experiments were conducted to quantify the underwater suction under various preloads (Qiao et al., 2018).

3.2.1. Zero liquid depth

We begin the discussion by first forming an understanding when $h = 0$, $p_0 = p_a$. Results for a hemispherical crater in air (blue) and underwater (red) at $h = 0$ are displayed in Figure 7A. It is obvious that craters of both fillings experience an increase in suction with growing preload, whereas the liquid-filled craters exhibit a faster increase due to the stronger constraint on the polymer matrix under volume conservation, i.e., $V_1 = V_2$, compared with the ideal gas relation, $p_1V_1 = p_2V_2$. Also, for both cases, FEM results (solid curves) are in excellent agreement with experiment (circular markers) when the preload is smaller than 80 kPa, while the two responses start~~s~~ to deviate as the preload further increases. For the crater in air, such a discrepancy can be successfully resolved by adding an experimentally extracted retraction strain in FEM (green open diamond markers in Figure 7A) because the strain at pull-off is ~~discernably~~ discernibly higher than the strain at full unloading when the specimen is subjected to large preload. For the crater underwater, however, the discrepancy could come from ~~the~~ vaporization of the liquid inside the crater when the internal pressure is extremely low or close to zero.

Figure 7B plots the normalized pressure drop obtained by FEM as a function of preload for both air-filled and liquid-filled hemispherical craters. The blue curve clearly shows that the pressure drop of the air-filled crater gradually increases with growing preload and eventually reaches a plateau of $-\Delta p = p_a$ when fully closed, i.e., vacuum, at $\sigma_f = 140$ kPa as highlighted by the vertical dashed magenta line. However, the crater underwater undergoes a faster pressure drop than those in air such that it reaches vacuum (i.e. $-\Delta p = p_a$) prior to the full closure. The intersection of the horizontal dashed black line of $-\Delta p = p_a$ and the curve of $-\Delta p/p_a(\sigma)$ determines a critical preload of $\sigma_v^0 = 80$ kPa. The critical preload suggests a threshold above which the liquid in the crater will vaporize. ~~In the simplest picture~~In other words, when $\sigma < \sigma_v^0$, the liquid inside the crater remains as an incompressible fluid, while when $\sigma \geq \sigma_v^0$, it should rapidly vaporize even ~~in~~ at room temperature. This liquid-to-gas phase transition violates the assumption of an incompressible fluid. Hence the FEM results beyond this point are no longer meaningful. It is also worth pointing out that when the craters are fully closed at $\sigma_f = 140$ kPa, the craters in air or water behave essentially the same as $-\Delta p = p_a$ is realized for both craters if $h = 0$. This explains the fully overlapped experimental results at $\sigma = \sigma_f$ as highlighted by the vertical magenta dashed line in Figure 7A.

3.2.2. Finite liquid depth

It is interesting to realize that the red curve in Figure 7B should be applicable to any $h > 0$ as long as both the polymer matrix and the liquid inside the crater are incompressible. This is because the hydrostatic pressure term $\rho g h$ in Eq. (5)~~(5)~~ has no effect on the deformation of the incompressible matrix. Different h's only dictate the critical preload for vaporization, σ_v, beyond which the FEM results are invalid. This can be understood by looking at the "phase diagram" in Figure 7C where the horizontal axis is the preload σ and the vertical axis is the normalized liquid depth $\rho g h/p_a$. The yellow regimes are non-vaporization zones in which the pressure drop is h-independent. The red regime is where vaporization is expected to occur. The cyan regime represents complete vacuum. Right before vaporization occurs, the pressure drop simply equals the ambient pressure i.e., $-\Delta p = p_a + \rho g h$. Thus, when $\sigma < \sigma_v^0$, no vaporization would take place for any h as p_2 is still positive after unloading. When $\sigma_v^0 \leq \sigma < \sigma_f$, we can introduce a function to represent the red curve in Figure 7B, say $-\Delta p/p_a(\sigma) = f(\sigma)$ for $0 < \sigma < \sigma_f$. Then σ_v can be obtained by solving $f(\sigma_v) = 1 + \rho g h/p_a$ for a given liquid depth h. If $\rho g h/p_a \geq f(\sigma) - 1$, the

liquid still remains incompressible fluid; otherwise, the liquid vaporizes. When $\sigma \geq \sigma_f$, the hemispherical crater attains full closure with complete vacuum, leading to $-\Delta p = p_a + \rho g h$. Therefore, when the crater is fully closed, craters in deeper water will produce a higher suction force.

In summary, craters underwater, on the one hand, are capable of producing higher suction force than those in air due to the volume constraints; on the other hand, vaporization may take place, which undermines the suction.

3.3. Isolated craters in air with surface tension

Up to this point, we neglected polymer surface tension, which may become important for small craters on a soft matrix. The significance of surface tension can be realized by examining molded polymer surfaces. A commonly adopted fabrication method for cratered surfaces is molding polymers out of a negative template, which are usually created using either micromachining (Choi et al., 2016) or colloidal lithography (Chang et al., 2014;Akerboom et al., 2015). Such methods work well for relatively stiff polymers such as UV resin (*E*~ GPa) (Chang et al., 2014) or even 10:1 PDMS (*E*~ MPa) (Akerboom et al., 2015). However, molding microscale craters on soft polymer sheet, e.g. 40:1 PDMS (*E*~100 kPa) (Choi et al., 2016), resulted in much smaller crater size compared with the domes on the template after demolding. This can be attributed to the so-called elasto-capillarity effects in which the polymer surface tension is a driving force for diminishing the sizes of craters when the crater length scale is comparable to the elasto-capillary length defined as $L_e = \gamma/E$ where γ is the surface tension of the polymer (Roman and Bico, 2010;Liu and Feng, 2012;Bico et al., 2018). To attain the desired crater shape, adding a stiffer reinforcing layer inside the crater has proven to be effective. The schematic of a reinforced crater is depicted in Figure 5D. The thickness and Young's modulus of the reinforcing layer are denoted as t and E_l, respectively. The effect of surface tension is equivalently interpreted as a normal traction $t_n = \kappa\gamma$ on the inner surface of the crater (shown by blue arrows), where κ is the sum of the two principal curvatures. To quantitatively characterize the effects of surface tension and reinforcing shell on the suction force generated by those craters, a demolding step was added prior to loading and unloading (Wang et al., 2017b). Therefore, the entire process of suction generation becomes demolding, loading, and unloading steps.

We investigated the surface tension effect by considering isolated hemi-spherical craters with reinforcements parameterized by their thickness and Young's modulus. A contour plot for the effective adhesive strength σ_{eff} as a function of normalized thickness t/a and modulus E_l/E is presented in Figure 8. It clearly suggests that there is an optimal combined range of t/a and E_l/E to generate large suction. When the reinforcing shell is too thin or too soft, it is simply too weak to resist the surface tension effect. When the reinforcing shell is too thick or too stiff, it preserves the crater shape after demolding, but it also prevents the crater from deformation during loading. As a result, a large V_1 leads to small σ_{eff} according to Eq. (4~~(4~~). The effect of strong and weak reinforcing shells is best visualized by the supplementary videos of (Wang et al., 2017b). Therefore, the optimal choice of t/a andE_l/E for large σ_{eff} lies in the domain $E_l/E \in (20,50)$ and $t/a \in (0.025,0.15)$ as shown by the red regime in Figure 8.

In fact, adding a reinforcing layer may even enhance the suction force for craters with negligible surface tension effects. ~~It~~ This is because a thin reinforcing layer can assist the crater to spring back upon unloading, while leaving the overall structural stiffness almost unchanged (Qiao et al., 2017). Surprisingly, a reinforced SCS crater with aspect ratio $b/a = 0.85$ shows a maximum $\sigma_{eff} = 1.2p_a$, which is higher than the atmospheric pressure because $A_2 > A_0$ is achieved due to wrinkling instabilities on the crater inner surface. Such a wrinkling instability is because of the stiffness mismatch between the reinforcing layer and the polymer matrix when being compressed. Although the wrinkled surface may enlarge the projected area of the crater after unloading, it is not easy to control, thus it is not within the scope of the current analysis. A detailed discussion can be found in (Qiao et al., 2017).

IV. Crater Arrays in Air

Isolated craters discussed in the previous section represent cratered surfaces with very small crater areal fraction, i.e., $\phi \to 0$, such that the interaction between craters is negligible. When craters are closely packed, the behavior of each crater may be affected by its neighboring craters. Actually, experimental evidence has shown that the crater areal fraction is another crucial geometric parameter that governs the adhesive strength. For example, Nanni *et al.* measured the adhesion of elastomeric surfaces structured with micro-dimples of different areal fractions (Figure

1K) (Nanni et al., 2015). They observed that the adhesive strength exhibits a non-monotonic dependence on the crater areal fraction. In addition to the areal fraction, different patterns of crater arrays have been reported such as hexagonal (Figures 1I and 1J) and square (Figure 1K). In this section, we briefly discuss our recent progress in simulating the suction effects in hexagonal-patterned arrays (HPA) and square-patterned arrays (SPA) with various ϕ's.

Consider two polymer sheets with the same total base plane area of A_t. Then the crater area fraction is defined as $\phi = A_0/A_t$. One is engineered with SPA (Figure 5E) and the other with HPA (Figure 5F). Different from simulations for isolated craters where axisymmetric models were used, simulations for crater arrays demand three-dimensional models and periodic boundary conditions. The suction force is still generated via the loading-unloading process as illustrated in Figure 6A. The normalized total suction force of the polymer sheet ($F_t/(p_0A_t)$) is obtained and plotted as a function of ϕ in Figure 9, where red represents HPA and blue SPA. Shaded bars correspond to a relatively small preload of 50 kPa and solid ones for a large preload of 120 kPa. Note that results presented in Figure 9 are for SCS crater arrays with crater aspect ratio of $b/a = 2/3$ and matrix Young's modulus of $E = 141.9$ kPa. The aspect ratio $b/a = 2/3$ is intentionally selected since the initial volume of a cylinder-shaped crater with $b/a = 2/3$ is identical to that of a SCS crater with aspect ratio $b/a = 1$. Figure 9 clearly shows that under a small preload of 50 kPa (shaded bars), the total suction force increases with growing ϕ. The reason is twofold. First, crater arrays with large ϕ tend to have lower structural stiffness, leading to a larger deformation under the same preload, i.e., small V_1 produces large F according to Eq. (3)~~(3)~~. Second, large ϕ means more craters are contributing to F_t. However, under a large preload, e.g. 120 kPa, the total suction force exhibits a non-monotonic dependence on ϕ and the maximum is achieved when $\phi \in (54.5\%, 64.9\%)$. This is because, when $\sigma = 120$ kPa, craters are fully closed after loading and craters with large ϕ may not recover after unloading due to low structural stiffness. Therefore, one can conclude that the interaction between craters may impair the overall adhesive strength of the polymer sheet under large preload. This non-monotonic trend is essentially similar to the experimental observation reported by Nanni *et al* (Nanni et al., 2015). It is also worth noting that the difference between SPA and HPA is not significant for the same ϕ according to Figure 9.

V. Summary and Outlooks

~~Reversible~~ Progress in the development of reversible SDAs ~~is~~ has been ~~a field undergoing~~ rapid ~~development~~. So far, micro-pillared surfaces have been regarded as the primary option. In this review, we focus on cratered surfaces as an alternative, with the emphasis on our recent mechanistic understandings of suction effects of craters arrays. Through theoretical analysis, numerical simulation, and experimental measurements, the effect of polymer matrix stiffness, crater shape, air/water ambient environments, elasto-capillarity, crater area fraction, and pattern of crater arrays are systematically studied.

However, there is a major limitation in the present modeling framework, related to the simplified loading-unloading process for realizing suction effects as illustrated by Figures 6A-6C. First, the substrate is assumed to be rigid and the crater/substrate interface is assumed to be frictionless. Deformable substrates (e.g., skin) and interfacial friction may prevent the venting of air/liquid during loading, and thus diminish the suction effects. Second, effective venting during loading and tight sealing during unloading and beyond, play crucial roles in strong and sustained adhesion, which should be a future direction for the design of cratered surfaces. Moreover, existing models cannot explain the experimental findings that even with exactly the same crater shape, areal fraction, and pattern, crater arrays may still exhibit different adhesive strength when the size of the crater varies (Baik et al., 2017). This size effect (not pertaining to elasto-capilarity) remains unresolved. In addition to passive cratered surfaces, reversible suction-based adhesion can also be enabled by active materials in response to external stimuli, such as temperature (Lee et al., 2016) or magnetic field (Yu et al., 2018;Linghu et al., 2019), which have not been systematically modeled.

Another potential direction for future work is to employ cohesive zone modeling in the analysis of the performance of cratered surfaces. This would allow for the intrinsic interactions (normal and shear) between contacting surfaces to be accounted for. In addition, such an approach would allow the strength and adhesion energy of different configurations to be compared, rather than relying solely on strength comparisons, which is the current practice. There may be performance regimes that are strength controlled and others that are dominated by energy considerations. This could result in the development of a richer parameter space for exploring the performance of cratered surfaces.

In summary, cratered surfaces represent a new class of SDAs with strong adhesion, remarkable reusability, and superior biocompatibility. After about six years of studies, research into the performance of cratered SDAs are still in its infancy. Preliminiary understandings summarized in this review were achieved under many simplifications and assumptions. The mechanics and realization of practically useful cratered SDAs are still elusive with wide open oppurtunities. ~~The~~ Our understanding of the underlying mechanisms, exploration of optimal design, and employment of active materials require the collective wisdom of both mechanical engineers and material scientists.

Author Contributions

L. Wang, K. Ha, G.J. Rodin, K. Liechti, N. Lu participated fully to the data acquisition, analysis, and paper writing. All authors contributed to the article and approved the submitted version.

Conflict of Interest

The authors declare that the research was conducted in the absence of any commercial or financial relationships that could be construed as a potential conflict of interest.

Acknowledgements All authors acknowledge the support from the National Science Foundation (NSF) Division of Civil, Mechanical and Manufacturing Innovation (CMMI) award (Grant No. 1663551). Liu Wang acknowledges the Warren A. and Alice L. Meyer endowed graduate fellowship awarded by the Cockrell School of Engineering at the University of Texas at Austin. Kyoung-Ho Ha acknowledges the Philip C. and Linda L. Lewis Foundation Graduate Fellowship in Mechanical Engineering at the University of Texas at Austin.

Table 1. Micro-Pillar-Enabled SDAs

Material	Modulus (MPa)	Normal Adhesion (kPa)	Tip diameter(μm)	Pillar length (μm)	Tip Shape	Reference
Polythiophene Nanotube	1500	800	0.2	12	Nanohair	(Lu et al., 2008)
Polyurethane	3	180	4.5	20	Mushroom	(Kim and Sitti, 2006)
Sylgard 184	1-10.	111-219	40	100	Mushroom	(Davies et al., 2009)
MWCNT	10E5	117	0.02-0.03	5-10.	Fiber	(Zhao et al., 2006)
Sylgard 184	1-10	100-180	10	20	Mushroom	(Sameoto and Menon, 2009)
Gecko (β –keratin)	1500	100			Hierarchical	(Autumn et al., 2000)
Sylgard 184	0.76	5	10	30	Mushroom	(Del Campo et al., 2007b)
Graded PDMS	5.	92.5	2	2	Round	(Tsai and Chang, 2013)
Polyurethane	2.9	24	50	100	Mushroom	(Cheung and Sitti, 2009)
Polyurethane	3	50	35	100	Tilted	(Murphy et al., 2009)
Polyimide	2500	30	0.2-4	0.15-2	Fiber	(Geim et al., 2003)
PDMS	2-3	22.5	20	55	Mushroom	(Hu et al., 2017)
PDMS	2	13	5	5-20.	Mushroom	(Kwak et al., 2011)
PDMS	1.5-3.5	13	5	30	Mushroom	(Kim et al., 2016)
PDMS	2-3.	12.5	13	80	Tilted	(Jin et al., 2014)
PDMS	2-3.	10.5		100	Wedge	(Tao et al., 2017)
PDMS	2.8-8.2	7.5-18	5	20	Mushroom	(Bae et al., 2013)
PDMS	2-3.	7.5-14	60-95	120	Mushroom	(Drotlef et al., 2017)
Silicones	1.75-2.63	5.1	50	200	Wedge	(Parness et al., 2009)
Silicone rubber	0.57	0.028	0.2	60	Fiber	(Sitti and Fearing, 2003)

Table 2. Crater-Enabled SDAs

Material	Modulus (MPa)	Shape	Ambient condition	Diameter (μm)	Normal Adhesion (kPa)	Reference
s-PUA	1.5	Protuberance	In Air	30	15	(Baik et al., 2017)
				100	26	
				300	25	
			Underwater	30	25	
				100	42	
				300	15	
PDMS	0.8	Concave	In Air	30	20	(Baik et al., 2018)
				100	30	
				1000	8	
			Underwater	30	32	
				100	115	
				1000	55	
	2.2	Concave with rim	In Air	5	13	(Oh et al., 2018)
	0.5	Protuberance	In Air	30	60	(Kim et al., 2019)
			Underwater		45	
	0.2		In Air	30	18	(Chun et al., 2018)
			Underwater		13	
PDMS	0.105	Concave	In Air	1	1.5	(Choi et al., 2016)

Figure Captions

Figure 1 Examples of nature-inspired SDAs. (A)-(E) Gecko-inspired synthetic micro-pillars with various tip geometries: (A) flat tip (reprinted with permission from ref (Del Campo et al., 2007b)); (B) hierarchical tip (reprinted with permission from ref (Greiner et al., 2009)); (C) spatular tip (reprinted with permission from ref (Del Campo and Arzt, 2007)); (D) slanted tip (reprinted with permission from ref (Murphy et al., 2009)); (E) mushroom-like tip (reprinted with permission from ref (Wang et al., 2014)). (f) A combinational structure – micro-pillars with concave tip (reprinted with permission from ref (Baik et al., 2018)). (G)-(K) Octopus-inspired synthetic micro-suckers or craters: (G) nano-craters on UV resin surfaces (reprinted with permission from ref (Chang et al., 2014)); (H) reversible adhesive skin patch with micro-craters on multilayer PDMS (reprinted with permission from ref (Choi et al., 2016)); (I) micro-craters on PDMS surface (reprinted with permission from ref(Akerboom et al., 2015)); (J) micro-craters with interior protuberances (reprinted with permission from ref (Baik et al., 2017)); (K) square-patterned micro-craters on PDMS surface (reprinted with permission from ref (Nanni et al., 2015)). (L) Another combinational structure – pillar with funnel-shaped tip (reprinted with permission from ref (Fischer et al., 2017)).

Figure 2 Limitations of pillared surfaces and advantages of cratered surfaces as SDAs. (A) A scanning electron microscopy (SEM) image of pillar condensation. (reprinted with permission from ref (Kim et al., 2007)). (B) Adhesion force of micro-pillars as a function of relative humidity (reprinted with permission from ref (Cadirov et al., 2017)). (C) Adhesive strengths of various pillared and cratered structures where red: protuberance-shaped crater; blue: perforated cylinders; green: cylindrical pillar; brown: cylindrical hole; black: flat surface (reprinted with permission from ref (Baik et al., 2017)). (D) Repeatable adhesion of the crater-enabled SDAs after more than 10000 cycles of attachment and detachment (reprinted with permission from ref (Baik et al., 2017)).

Figure 3 An Ashby plot of normal adhesive strength vs. material Young's modulus for both pillar-enabled and crater-enabled SDAs. Purple regimes enclose data of pillared surfaces in air. The orange regime denotes craters in air and the green regime represents craters underwater.

Figure 4 Suction cup example applications and models. (A) Wall-climbing robots with suction cups as attaching components (reprinted with permission from ref (Yoshida and Ma, 2010)). (B) A suction-cup-based tapered soft actuator capabile of gripping objects of various shapes (reprinted with permission from

ref (Xie et al., 2020)). (C) An organohydrogel-based soft gripper with electrically programmable stiffness for achieving conformable contact with rough surfaces. (reprinted with permission from ref (Zhuo et al., 2020)). (D) Schematics of a pressing-detaching process of a suction cup (reprinted with permission from ref (Ge et al., 2015)).

Figure 5 Six factors that affect the suction effects of crater arrays discussed in this review article: (A) matrix modulus; (B) crater shape, (C) ambient environment; (D) elasto-capillarity at small length scale; (E) crater area fraction; (F) the pattern of a crater array.

Figure 6 The model of a macroscopic, isolated crater in air. (A)-(C) Schematics of the loading-unloading process that generates suction. (D) An axisymmetric finite element model (FEM) for simulating isolated craters. (E) A representative loading-unloading-retraction curve for a cratered specimen. The inset shows the experimental setup. (F) Effective adhesive strength as a function of the preload for spherical-cap-shaped (SCS) craters with aspect ratios $b/a = 2/3$ and 1. (G) A contour plot for effective adhesive strength σ_{eff} as a function of the matrix Young's modulus E and crater aspect ratio b/a. (reprinted with permission from(Qiao et al., 2017))

Figure 7 Experimental and modeling results for craters underwater. (A) Effective adhesive strength σ_{eff} as a function of preload σ for craters in air (blue) and underwater (red). Curves are FEM results at the unloading point. Solid markers are experimental results and open diamond markers are FEM results at the pull-off point. (B) Pressure drop as a function of preload σ. For craters filled with liquid, when internal pressure approaches zero, rapid vaporization can happen at room temperature, which violates the incompressible fluid assumption. (C) Phase diagram of pressure drop as a function of liquid depth h and preload σ. (reprinted with permission from(Qiao et al., 2018))

Figure 8. A contour plot of effective adhesive strength σ_{eff} as a function of normalized thickness and Young' modulus of the reinforcing layer. Results are obtained under full closure with an elasto-capillary number $\gamma/(Ea) = 1/3$. (reprinted with permission from(Wang et al., 2017b))

Figure 9 Normalized total suction force $F_t/(p_0 A_t)$ as a function of crater area fraction ϕ for crater arrays with fixed crater shape (SCS with $b/a = 2/3$) and matrix Young's modulus E = 141.9 kPa. Red represents hexagonal pattern arrays (HPA) and blue for square-patterned arrays (SPA). Shaded bars are for small preload case (σ = 50 ~~MPa~~kPa) and solid bars are for large preload case (σ = 120 ~~MPa~~kPa). (reprinted with permission from(Wang et al., 2019))

References

Afferrante, L., and Carbone, G. (2012). Biomimetic surfaces with controlled direction-dependent adhesion. *Journal of The Royal Society Interface* 9, 3359-3365.

Akerboom, S., Appel, J., Labonte, D., Federle, W., Sprakel, J., and Kamperman, M. (2015). Enhanced adhesion of bioinspired nanopatterned elastomers via colloidal surface assembly. *J R Soc Interface* 12, 20141061.

Aksak, B., Murphy, M.P., and Sitti, M. (~~Year~~2008). "Gecko inspired micro-fibrillar adhesives for wall climbing robots on micro/nanoscale rough surfaces", in: *Robotics and Automation, 2008. ICRA 2008. IEEE International Conference on*: IEEE), 3058-3063.

Arzt, E., Gorb, S., and Spolenak, R. (2003). From micro to nano contacts in biological attachment devices. *Proceedings of the National Academy of Sciences* 100, 10603-10606.

Autumn, K., Dittmore, A., Santos, D., Spenko, M., and Cutkosky, M. (2006a). Frictional adhesion: a new angle on gecko attachment. *Journal of Experimental Biology* 209, 3569-3579.

Autumn, K., Liang, Y.A., Hsieh, S.T., Zesch, W., Chan, W.P., Kenny, T.W., Fearing, R., and Full, R.J. (2000). Adhesive force of a single gecko foot-hair. *Nature* 405, 681-685.

Autumn, K., Majidi, C., Groff, R., Dittmore, A., and Fearing, R. (2006b). Effective elastic modulus of isolated gecko setal arrays. *Journal of Experimental Biology* 209, 3558-3568.

Autumn, K., Sitti, M., Liang, Y.A., Peattie, A.M., Hansen, W.R., Sponberg, S., Kenny, T.W., Fearing, R., Israelachvili, J.N., and Full, R.J. (2002). Evidence for van der Waals adhesion in gecko setae. *Proceedings of the National Academy of Sciences* 99, 12252-12256.

Bae, W.G., Kim, D., Kwak, M.K., Ha, L., Kang, S.M., and Suh, K.Y. (2013). Enhanced Skin Adhesive Patch with Modulus-Tunable Composite Micropillars. *Advanced healthcare materials* 2, 109-113.

Baik, S., Kim, D.W., Park, Y., Lee, T.-J., Ho Bhang, S., and Pang, C. (2017). A wet-tolerant adhesive patch inspired by protuberances in suction cups of octopi. *Nature* 546, 396-400.

Baik, S., Kim, J., Lee, H.J., Lee, T.H., and Pang, C. (2018). Highly Adaptable and Biocompatible Octopus-Like Adhesive Patches with Meniscus-Controlled Unfoldable 3D Microtips for Underwater Surface and Hairy Skin. *Advanced Science*, 1800100.

Baik, S., Lee, H.J., Kim, D.W., Kim, J.W., Lee, Y., and Pang, C. (2019a). Bioinspired Adhesive Architectures: From Skin Patch to Integrated Bioelectronics. *Adv Mater* 0, e1803309.

Baik, S., Lee, H.J., Kim, D.W., Min, H., and Pang, C. (2019b). A capillarity-enhanced organ-attachable adhesive with highly drainable wrinkled octopus-inspired architectures. *ACS applied materials & interfaces*.

Baik, S., Lee, H.J., Kim, D.W., Min, H., and Pang, C. (2019c). Capillarity-Enhanced Organ-Attachable Adhesive with Highly Drainable Wrinkled Octopus-Inspired Architectures. *ACS Applied Materials & Interfaces*.

Bartlett, M.D., Croll, A.B., King, D.R., Paret, B.M., Irschick, D.J., and Crosby, A.J. (2012). Looking beyond fibrillar features to scale gecko-like adhesion. *Advanced Materials* 24, 1078-1083.

Bartlett, M.D., and Crosby, A.J. (2014). High capacity, easy release adhesives from renewable materials. *Advanced Materials* 26, 3405-3409.

Becker, H., and Heim, U. (2000). Hot embossing as a method for the fabrication of polymer high aspect ratio structures. *Sensors and Actuators A: Physical* 83, 130-135.

Bico, J., Reyssat, É., and Roman, B. (2018). Elastocapillarity: When Surface Tension Deforms Elastic Solids. *Annual Review of Fluid Mechanics*.

Brodoceanu, D., Bauer, C.T., Kroner, E., Arzt, E., and Kraus, T. (2016). Hierarchical bioinspired adhesive surfaces—a review. *Bioinspiration & Biomimetics* 11, 051001.

Buhl, S., Greiner, C., Campo, A.D., and Arzt, E. (2009). Humidity influence on the adhesion of biomimetic fibrillar surfaces. *International Journal of Materials Research* 100, 1119-1126.

Cadirov, N., Booth, J.A., Turner, K.L., and Israelachvili, J.N. (2017). Influence of Humidity on Grip and Release Adhesion Mechanisms for Gecko-Inspired Microfibrillar Surfaces. *ACS Appl Mater Interfaces* 9**,** 14497-14505.

Carbone, G., and Pierro, E. (2012). Sticky Bio-inspired Micropillars: Finding the Best Shape. *Small* 8**,** 1449-1454.

Carbone, G., Pierro, E., and Gorb, S.N. (2011). Origin of the superior adhesive performance of mushroom-shaped microstructured surfaces. *Soft Matter* 7**,** 5545-5552.

Chan, E.P., Greiner, C., Arzt, E., and Crosby, A.J. (2007). Designing model systems for enhanced adhesion. *MRS bulletin* 32**,** 496-503.

Chang, W.-Y., Wu, Y., and Chung, Y.-C. (2014). Facile fabrication of ordered nanostructures from protruding nanoballs to recessional nanosuckers via solvent treatment on covered nanosphere assembled monolayers. *Nano letters* 14**,** 1546-1550.

Chary, S., Tamelier, J., and Turner, K. (2013). A microfabricated gecko-inspired controllable and reusable dry adhesive. *Smart Materials and Structures* 22**,** 025013.

Chen, X., Yuk, H., Wu, J., Nabzdyk, C.S., and Zhao, X. (2020a). Instant tough bioadhesive with triggerable benign detachment. *Proceedings of the National Academy of Sciences* 117**,** 15497-15503.

Chen, Y., Meng, J., Gu, Z., Wan, X., Jiang, L., and Wang, S. (2020b). Bioinspired Multiscale Wet Adhesive Surfaces: Structures and Controlled Adhesion. *Advanced Functional Materials* 30**,** 1905287.

Cheung, E., and Sitti, M. (2009). Adhesion of biologically inspired polymer microfibers on soft surfaces. *Langmuir* 25**,** 6613-6616.

Cho, H., Wu, G., Jolly, J.C., Fortoul, N., He, Z., Gao, Y., Jagota, A., and Yang, S. (2019). Intrinsically reversible superglues via shape adaptation inspired by snail epiphragm. *Proceedings of the National Academy of Sciences* 116**,** 13774-13779.

Choi, M.K., Park, O.K., Choi, C., Qiao, S., Ghaffari, R., Kim, J., Lee, D.J., Kim, M., Hyun, W., Kim, S.J., Hwang, H.J., Kwon, S.H., Hyeon, T., Lu, N., and Kim, D.H. (2016). Cephalopod-Inspired Miniaturized Suction Cups for Smart Medical Skin. *Adv Healthc Mater* 5**,** 80-87.

Christoffers, W.A., Coenraads, P.J., and Schuttelaar, M.L. (2014). Bullous allergic reaction caused by colophonium in medical adhesives. *Contact dermatitis* 70**,** 256-257.

Chun, S., Kim, D.W., Baik, S., Lee, H.J., Lee, J.H., Bhang, S.H., and Pang, C. (2018). Conductive and Stretchable Adhesive Electronics with Miniaturized Octopus-Like Suckers against Dry/Wet Skin for Biosignal Monitoring. *Advanced Functional Materials* 28**,** 1805224.

Cilurzo, F., Gennari, C.G., and Minghetti, P. (2012). Adhesive properties: a critical issue in transdermal patch development. *Expert opinion on drug delivery* 9**,** 33-45.

Creton, C. (2003). Pressure-sensitive adhesives: an introductory course. *MRS bulletin* 28**,** 434-439.

Czech, Z., and Kowalczyk, A. (2011). "Pressure-sensitive adhesives for medical applications," in *Wide Spectra of Quality Control*. InTech).

Czech, Z., Wilpiszewska, K., Tyliszczak, B., Jiang, X., Bai, Y., and Shao, L. (2013). Biodegradable self-adhesive tapes with starch carrier. *International Journal of Adhesion and Adhesives* 44**,** 195-199.

Davies, J., Haq, S., Hawke, T., and Sargent, J. (2009). A practical approach to the development of a synthetic Gecko tape. *International Journal of Adhesion and Adhesives* 29**,** 380-390.

Del Campo, A., and Arzt, E. (2007). Design parameters and current fabrication approaches for developing bioinspired dry adhesives. *Macromolecular bioscience* 7**,** 118-127.

Del Campo, A., Greiner, C., Álvarez, I., and Arzt, E. (2007a). Patterned surfaces with pillars with controlled 3 D tip geometry mimicking bioattachment devices. *Advanced Materials* 19**,** 1973-1977.

Del Campo, A., Greiner, C., and Arzt, E. (2007b). Contact shape controls adhesion of bioinspired fibrillar surfaces. *Langmuir* 23**,** 10235-10243.

Drotlef, D.M., Amjadi, M., Yunusa, M., and Sitti, M. (2017). Bioinspired composite microfibers for skin adhesion and signal amplification of wearable sensors. *Advanced Materials* 29**,** 1701353.

Drotlef, D.M., Dayan, C.B., and Sitti, M. (2019). Bio-inspired Composite Microfibers for Strong and Reversible Adhesion on Smooth Surfaces. *Integr Comp Biol*.

Eisenhaure, J., and Kim, S. (2017). A review of the state of dry adhesives: biomimetic structures and the alternative designs they inspire. *Micromachines* 8**,** 125.
Fischer, S.C., Arzt, E., and Hensel, R. (2016). Composite pillars with a tunable interface for adhesion to rough substrates. *ACS applied materials & interfaces* 9**,** 1036-1044.
Fischer, S.C., Groß, K., Torrents Abad, O., Becker, M.M., Park, E., Hensel, R., and Arzt, E. (2017). Funnel-Shaped Microstructures for Strong Reversible Adhesion. *Advanced Materials Interfaces* 4**,** 1700292.
Gao, H., and Yao, H. (2004). Shape insensitive optimal adhesion of nanoscale fibrillar structures. *Proceedings of the National Academy of Sciences of the United States of America* 101**,** 7851-7856.
Ge, D., Matsuno, T., Sun, Y., Ren, C., Tang, Y., and Ma, S. (2015). Quantitative study on the attachment and detachment of a passive suction cup. *Vacuum* 116**,** 13-20.
Geim, A.K., Dubonos, S.V., Grigorieva, I.V., Novoselov, K.S., Zhukov, A.A., and Shapoval, S.Y. (2003). Microfabricated adhesive mimicking gecko foot-hair. *Nat Mater* 2**,** 461-463.
Gorb, S.N., Sinha, M., Peressadko, A., Daltorio, K.A., and Quinn, R.D. (2007). Insects did it first: a micropatterned adhesive tape for robotic applications. *Bioinspiration & Biomimetics* 2**,** S117-S125.
Greiner, C., Arzt, E., and Del Campo, A. (2009). Hierarchical Gecko-Like Adhesives. *Advanced Materials* 21**,** 479-482.
Greiner, C., Campo, A.D., and Arzt, E. (2007). Adhesion of bioinspired micropatterned surfaces: effects of pillar radius, aspect ratio, and preload. *Langmuir* 23**,** 3495-3502.
Hansen, W.R., and Autumn, K. (2005). Evidence for self-cleaning in gecko setae. *Proc Natl Acad Sci U S A* 102**,** 385-389.
Hu, H., Tian, H., Shao, J., Li, X., Wang, Y., Wang, Y., Tian, Y., and Lu, B. (2017). Discretely Supported Dry Adhesive Film Inspired by Biological Bending Behavior for Enhanced Performance on a Rough Surface. *ACS applied materials & interfaces* 9**,** 7752-7760.
Huber, G., Orso, S., Spolenak, R., Wegst, U.G., Enders, S., Gorb, S.N., and Arzt, E. (2008). Mechanical properties of a single gecko seta. *International journal of materials research* 99**,** 1113-1118.
Hwang, I., Kim, H.N., Seong, M., Lee, S.H., Kang, M., Yi, H., Bae, W.G., Kwak, M.K., and Jeong, H.E. (2018). Multifunctional Smart Skin Adhesive Patches for Advanced Health Care. *Advanced healthcare materials***,** 1800275.
Iwasaki, H., Lefevre, F., Damian, D.D., Iwase, E., and Miyashita, S. (2020). Autonomous and Reversible Adhesion Using Elastomeric Suction Cups for In-Vivo Medical Treatments. *IEEE Robotics and Automation Letters* 5**,** 2015-2022.
Jin, K., Cremaldi, J.C., Erickson, J.S., Tian, Y., Israelachvili, J.N., and Pesika, N.S. (2014). Biomimetic bidirectional switchable adhesive inspired by the gecko. *Advanced Functional Materials* 24**,** 574-579.
Kamperman, M., Kroner, E., Del Campo, A., Mcmeeking, R.M., and Arzt, E. (2010). Functional adhesive surfaces with "gecko" effect: The concept of contact splitting. *Advanced Engineering Materials* 12**,** 335-348.
Kawahara, K., and Tojo, K. (2007). Skin irritation in transdermal drug delivery systems: A strategy for its reduction. *Pharmaceutical research* 24**,** 399.
Kier, W.M., and Smith, A.M. (2002). The structure and adhesive mechanism of octopus suckers. *Integrative and Comparative Biology* 42**,** 1146-1153.
Kim, D.S., Lee, H.S., Lee, J., Kim, S., Lee, K.-H., Moon, W., and Kwon, T.H.J.M.T. (2007). Replication of high-aspect-ratio nanopillar array for biomimetic gecko foot-hair prototype by UV nano embossing with anodic aluminum oxide mold. 13**,** 601-606.
Kim, D.W., Baik, S., Min, H., Chun, S., Lee, H.J., Kim, K.H., Lee, J.Y., and Pang, C. (2019). Highly Permeable Skin Patch with Conductive Hierarchical Architectures Inspired by Amphibians and Octopi for Omnidirectionally Enhanced Wet Adhesion. *Advanced Functional Materials* 0**,** 1807614.
Kim, S., and Sitti, M. (2006). Biologically inspired polymer microfibers with spatulate tips as repeatable fibrillar adhesives. *Applied physics letters* 89**,** 261911.

Kim, T., Park, J., Sohn, J., Cho, D., and Jeon, S. (2016). Bioinspired, Highly Stretchable, and Conductive Dry Adhesives Based on 1D-2D Hybrid Carbon Nanocomposites for All-in-One ECG Electrodes. *Acs Nano* 10**,** 4770-4778.

Kwak, M.K., Jeong, H.E., and Suh, K.Y. (2011). Rational design and enhanced biocompatibility of a dry adhesive medical skin patch. *Adv Mater* 23**,** 3949-3953.

Lee, H., Um, D.S., Lee, Y., Lim, S., Kim, H.J., and Ko, H. (2016). Octopus-Inspired Smart Adhesive Pads for Transfer Printing of Semiconducting Nanomembranes. *Advanced Materials* 28**,** 7457-7465.

Lee, J., Fearing, R.S., and Komvopoulos, K. (2008). Directional adhesion of gecko-inspired angled microfiber arrays. *Applied Physics Letters* 93**,** 191910.

Li, Y., Krahn, J., and Menon, C. (2016). Bioinspired dry adhesive materials and their application in robotics: A review. *Journal of Bionic Engineering* 13**,** 181-199.

Linghu, C., Wang, C., Cen, N., Wu, J., Lai, Z., and Song, J. (2019). Rapidly tunable and highly reversible bio-inspired dry adhesion for transfer printing in air and a vacuum. *Soft matter* 15**,** 30-37.

Liu, J.-L., and Feng, X.-Q. (2012). On elastocapillarity: A review. *Acta Mechanica Sinica* 28**,** 928-940.

Liu, J., Tanaka, K., Bao, L., and Yamaura, I. (2006). Analytical modelling of suction cups used for window-cleaning robots. *Vacuum* 80**,** 593-598.

Lu, G., Hong, W., Tong, L., Bai, H., Wei, Y., and Shi, G. (2008). Drying enhanced adhesion of polythiophene nanotubule arrays on smooth surfaces. *ACS nano* 2**,** 2342-2348.

Ma, Y., Ma, S., Wu, Y., Pei, X., Gorb, S.N., Wang, Z., Liu, W., and Zhou, F. (2018). Remote Control over Underwater Dynamic Attachment/Detachment and Locomotion. 30**,** 1801595.

Manabe, R., Suzumori, K., and Wakimoto, S. (~~Year~~2012). "A functional adhesive robot skin with integrated micro rubber suction cups", in: *Robotics and Automation (ICRA), 2012 IEEE International Conference on*: IEEE), 904-909.

Marvi, H., Song, S., and Sitti, M. (2015). Experimental investigation of optimal adhesion of mushroomlike elastomer microfibrillar adhesives. *Langmuir* 31**,** 10119-10124.

Matsumura, H., Ahmatjan, N., Ida, Y., Imai, R., and Wanatabe, K. (2013). A model for quantitative evaluation of skin damage at adhesive wound dressing removal. *International wound journal* 10**,** 291-294.

Mengüç, Y., Yang, S.Y., Kim, S., Rogers, J.A., and Sitti, M. (2012). Gecko-Inspired Controllable Adhesive Structures Applied to Micromanipulation. *Advanced Functional Materials* 22**,** 1246-1254.

Moon, M.-W., Cha, T.-G., Lee, K.-R., Vaziri, A., and Kim, H.-Y. (2010). Tilted Janus polymer pillars. *Soft Matter* 6**,** 3924-3929.

Murphy, M.P., Aksak, B., and Sitti, M. (2009). Gecko-Inspired Directional and Controllable Adhesion. *Small* 5**,** 170-175.

Nanni, G., Fragouli, D., Ceseracciu, L., and Athanassiou, A. (2015). Adhesion of elastomeric surfaces structured with micro-dimples. *Applied Surface Science* 326**,** 145-150.

Oh, J.H., Hong, S.Y., Park, H., Jin, S.W., Jeong, Y.R., Oh, S.Y., Yun, J., Lee, H., Kim, J.W., and Ha, J.S. (2018). Fabrication of High-Sensitivity Skin-Attachable Temperature Sensors with Bioinspired Microstructured Adhesive. *ACS applied materials & interfaces* 10**,** 7263-7270.

Parness, A., Soto, D., Esparza, N., Gravish, N., Wilkinson, M., Autumn, K., and Cutkosky, M. (2009). A microfabricated wedge-shaped adhesive array displaying gecko-like dynamic adhesion, directionality and long lifetime. *Journal of the Royal Society Interface*, rsif. 2009.0048.

Pattantyus-Abraham, A., Krahn, J., and Menon, C. (2013). Recent Advances in Nanostructured Biomimetic Dry Adhesives. *Frontiers in Bioengineering and Biotechnology* 1.

Pease, R. (1981). Electron beam lithography. *Contemporary Physics* 22**,** 265-290.

Pesika, N.S., Zeng, H., Kristiansen, K., Zhao, B., Tian, Y., Autumn, K., and Israelachvili, J. (2009). Gecko adhesion pad: a smart surface? *Journal of Physics: Condensed Matter* 21**,** 464132.

Qiao, S., Gratadour, J.-B., Wang, L., and Lu, N. (2015). Conformability of a thin elastic membrane laminated on a rigid substrate with corrugated surface. *IEEE Transactions on Components, Packaging and Manufacturing Technology* 5**,** 1237-1243.

Qiao, S., Wang, L., Ha, K.-H., and Lu, N. (2018). Suction effects of craters under water. *Soft Matter* 14, 8509-8520.

Qiao, S., Wang, L., Jeong, H., Rodin, G.J., and Lu, N. (2017). Suction effects in cratered surfaces. *Journal of The Royal Society Interface* 14, 20170377.

Roman, B., and Bico, J. (2010). Elasto-capillarity: deforming an elastic structure with a liquid droplet. *J. Phys.: Condens. Matter* 22, 493110.

Sahay, R., Low, H.Y., Baji, A., Shaohui, F., and Wood, K.L. (2015). A State-of-the-Art Review and Analysis on the Design of Dry Adhesion Materials for Applications such as Climbing Micro-robots. *RSC Advances*.

Sameoto, D., and Menon, C. (2009). A low-cost, high-yield fabrication method for producing optimized biomimetic dry adhesives. *Journal of Micromechanics and Microengineering* 19, 115002.

Seo, J., Eisenhaure, J., and Kim, S. (2016). Micro-wedge array surface of a shape memory polymer as a reversible dry adhesive. *Extreme Mechanics Letters* 9, 207-214.

Shintake, J., Cacucciolo, V., Floreano, D., and Shea, H.J.a.M. (2018). Soft Robotic Grippers. 1707035.

Singh, A.K., Mehra, D.S., Niyogi, U.K., Sabharwal, S., and Khandal, R.K. (2011). Polyurethane Based Pressure Sensitive Adhesives (PSAs) Using e-Beam Irradiation for Medical Application. *Journal of Polymer Materials* 28.

Singh, A.K., Mehra, D.S., Niyogi, U.K., Sabharwal, S., and Singh, G. (2014). Breathability studies of electron beam curable polyurethane pressure sensitive adhesive for bio-medical application. *Radiation Physics and Chemistry* 103, 75-83.

Sitti, M., and Fearing, R.S. (2003). Synthetic gecko foot-hair micro/nano-structures as dry adhesives. *Journal of adhesion science and technology* 17, 1055-1073.

Smith, A. (1996). Cephalopod sucker design and the physical limits to negative pressure. *Journal of Experimental Biology* 199, 949-958.

Smith, A.M. (1991). Negative pressure generated by octopus suckers: a study of the tensile strength of water in nature. *Journal of Experimental Biology* 157, 257-271.

Tao, D., Gao, X., Lu, H., Liu, Z., Li, Y., Tong, H., Pesika, N., Meng, Y., and Tian, Y. (2017). Controllable anisotropic dry adhesion in vacuum: gecko inspired wedged surface fabricated with ultraprecision diamond cutting. *Advanced Functional Materials* 27, 1606576.

Tinnemann, V., Hernández, L., Fischer, S.C., Arzt, E., Bennewitz, R., and Hensel, R. (2019). In Situ Observation Reveals Local Detachment Mechanisms and Suction Effects in Micropatterned Adhesives. *Advanced Functional Materials*, 1807713.

Tramacere, F., Appel, E., Mazzolai, B., and Gorb, S.N. (2014a). Hairy suckers: the surface microstructure and its possible functional significance in the Octopus vulgaris sucker. *Beilstein journal of nanotechnology* 5, 561-565.

Tramacere, F., Beccai, L., Kuba, M., Gozzi, A., Bifone, A., and Mazzolai, B. (2013). The morphology and adhesion mechanism of Octopus vulgaris suckers.

Tramacere, F., Kovalev, A., Kleinteich, T., Gorb, S.N., and Mazzolai, B. (2014b). Structure and mechanical properties of Octopus vulgaris suckers. *J R Soc Interface* 11, 20130816.

Tsai, C.-Y., and Chang, C.-C. (2013). Auto-adhesive transdermal drug delivery patches using beetle inspired micropillar structures. *J. Mater. Chem. B* 1, 5963-5970.

Varenberg, M., and Gorb, S. (2008). A beetle-inspired solution for underwater adhesion. *Journal of The Royal Society Interface* 5, 383-385.

Vieu, C., Carcenac, F., Pepin, A., Chen, Y., Mejias, M., Lebib, A., Manin-Ferlazzo, L., Couraud, L., and Launois, H. (2000). Electron beam lithography: resolution limits and applications. *Applied surface science* 164, 111-117.

Von Byern, J., and Klepal, W. (2006). Adhesive mechanisms in cephalopods: a review. *Biofouling* 22, 329-338.

Wang, L., Ha, K.-H., Qiao, S., and Lu, N. (2019). Suction effects of crater arrays. *Extreme Mechanics Letters* 30, 100496.

Wang, L., and Lu, N. (2016). Conformability of a thin elastic membrane laminated on a soft substrate with slightly wavy surface. *Journal of Applied Mechanics* 83**,** 041007.
Wang, L., Qiao, S., Ameri, S.K., Jeong, H., and Lu, N. (2017a). A Thin Elastic Membrane Conformed to a Soft and Rough Substrate Subjected to Stretching/Compression. *Journal of Applied Mechanics* 84**,** 111003.
Wang, L., Qiao, S., and Lu, N. (2017b). Effects of surface tension on the suction forces generated by miniature craters. *Extreme Mechanics Letters* 15**,** 130-138.
Wang, Y., Hu, H., Shao, J., and Ding, Y. (2014). Fabrication of well-defined mushroom-shaped structures for biomimetic dry adhesive by conventional photolithography and molding. *ACS Appl Mater Interfaces* 6**,** 2213-2218.
Wang, Y., Li, X., Tian, H., Hu, H., Tian, Y., Shao, J., and Ding, Y. (2015). Rectangle-capped and tilted micropillar array for enhanced anisotropic anti-shearing in biomimetic adhesion. *Journal of The Royal Society Interface* 12.
Wang, Y., Yang, X., Chen, Y., Wainwright, D.K., Kenaley, C.P., Gong, Z., Liu, Z., Liu, H., Guan, J., and Wang, T. (2017c). A biorobotic adhesive disc for underwater hitchhiking inspired by the remora suckerfish. *Science Robotics* 2**,** eaan8072.
Wang, Z. (2018). Slanted Functional Gradient Micropillars for Optimal Bioinspired Dry Adhesion. *ACS Nano*.
Xiaosong, L., Dashuai, T., Hongyu, L., Pengpeng, B., Zheyu, L., Liran, M., Yonggang, M., and Yu, T. (2019). Recent Developments in Gecko-inspired Dry Adhesive Surfaces from Fabrication to Application. *Surface Topography: Metrology and Properties*.
Xie, Z., Domel, A.G., An, N., Green, C., Gong, Z., Wang, T., Knubben, E.M., Weaver, J.C., Bertoldi, K., and Wen, L. (2020). Octopus Arm-Inspired Tapered Soft Actuators with Suckers for Improved Grasping. *Soft Robotics*.
Yao, H., and Gao, H. (2006). Mechanics of robust and releasable adhesion in biology: Bottom-up designed hierarchical structures of gecko. *Journal of the Mechanics and Physics of Solids* 54**,** 1120-1146.
Yoshida, Y., and Ma, S. (~~Year~~2010). "Design of a wall-climbing robot with passive suction cups", in: *2010 IEEE International Conference on Robotics and Biomimetics*: IEEE), 1513-1518.
Yu, Q., Chen, F., Zhou, H., Yu, X., Cheng, H., and Wu, H. (2018). Design and Analysis of Magnetic-Assisted Transfer Printing. *Journal of Applied Mechanics* 85**,** 101009.
Yuk, H., Varela, C.E., Nabzdyk, C.S., Mao, X., Padera, R.F., Roche, E.T., and Zhao, X. (2019). Dry double-sided tape for adhesion of wet tissues and devices. *Nature* 575**,** 169-174.
Zhao, Y., Tong, T., Delzeit, L., Kashani, A., Meyyappan, M., and Majumdar, A. (2006). Interfacial energy and strength of multiwalled-carbon-nanotube-based dry adhesive. *Journal of Vacuum Science & Technology B: Microelectronics and Nanometer Structures Processing, Measurement, and Phenomena* 24**,** 331-335.
Zhou, M., Pesika, N., Zeng, H., Tian, Y., and Israelachvili, J. (2013). Recent advances in gecko adhesion and friction mechanisms and development of gecko-inspired dry adhesive surfaces. *Friction* 1**,** 114-129.
Zhuo, S., Zhao, Z., Xie, Z., Hao, Y., Xu, Y., Zhao, T., Li, H., Knubben, E.M., Wen, L., Jiang, L., and Liu, M. (2020). Complex multiphase organohydrogels with programmable mechanics toward adaptive soft-matter machines. *Science Advances* 6**,** eaax1464.

Figure 1.JPEG

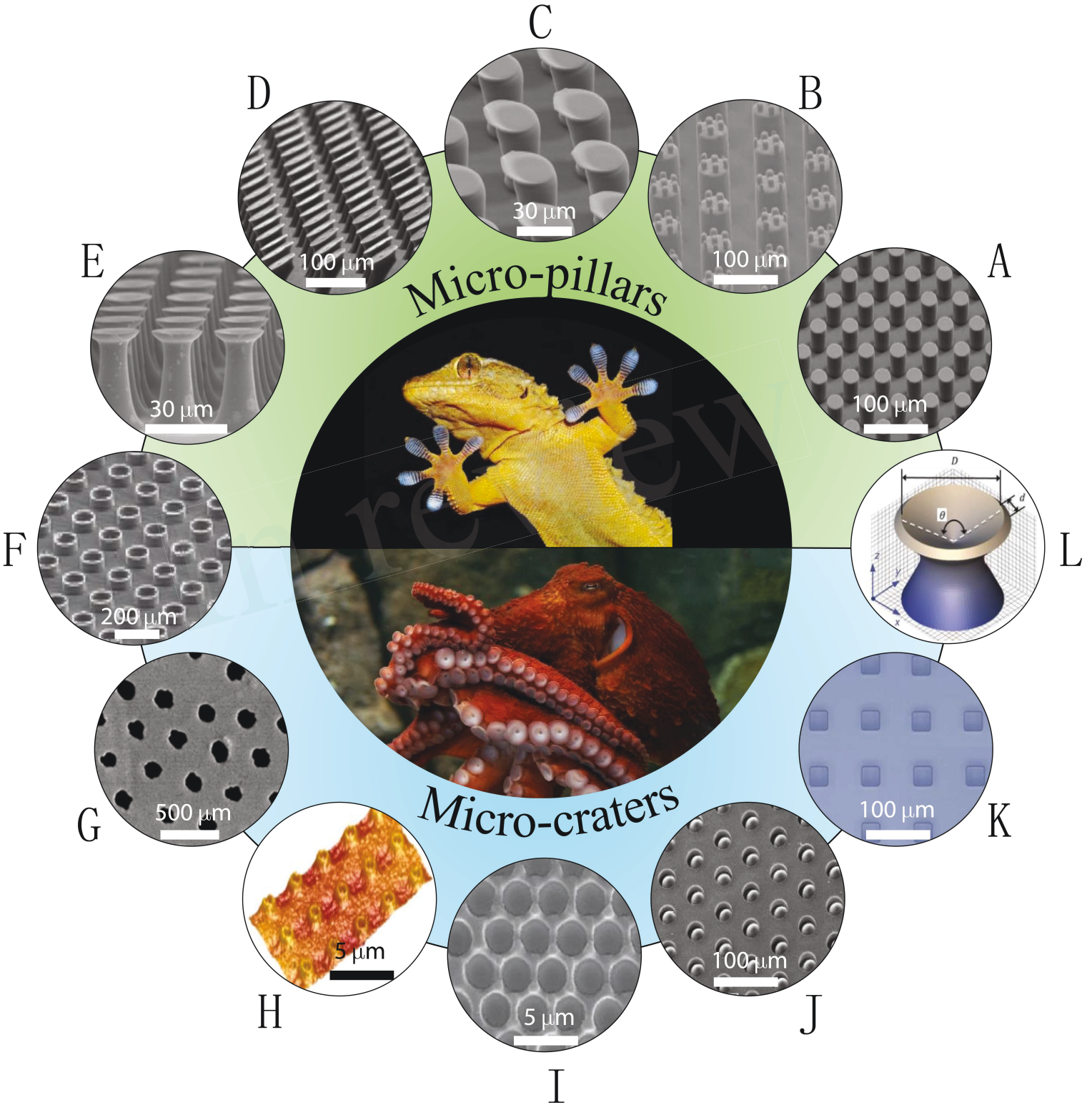

Figure 2.JPEG

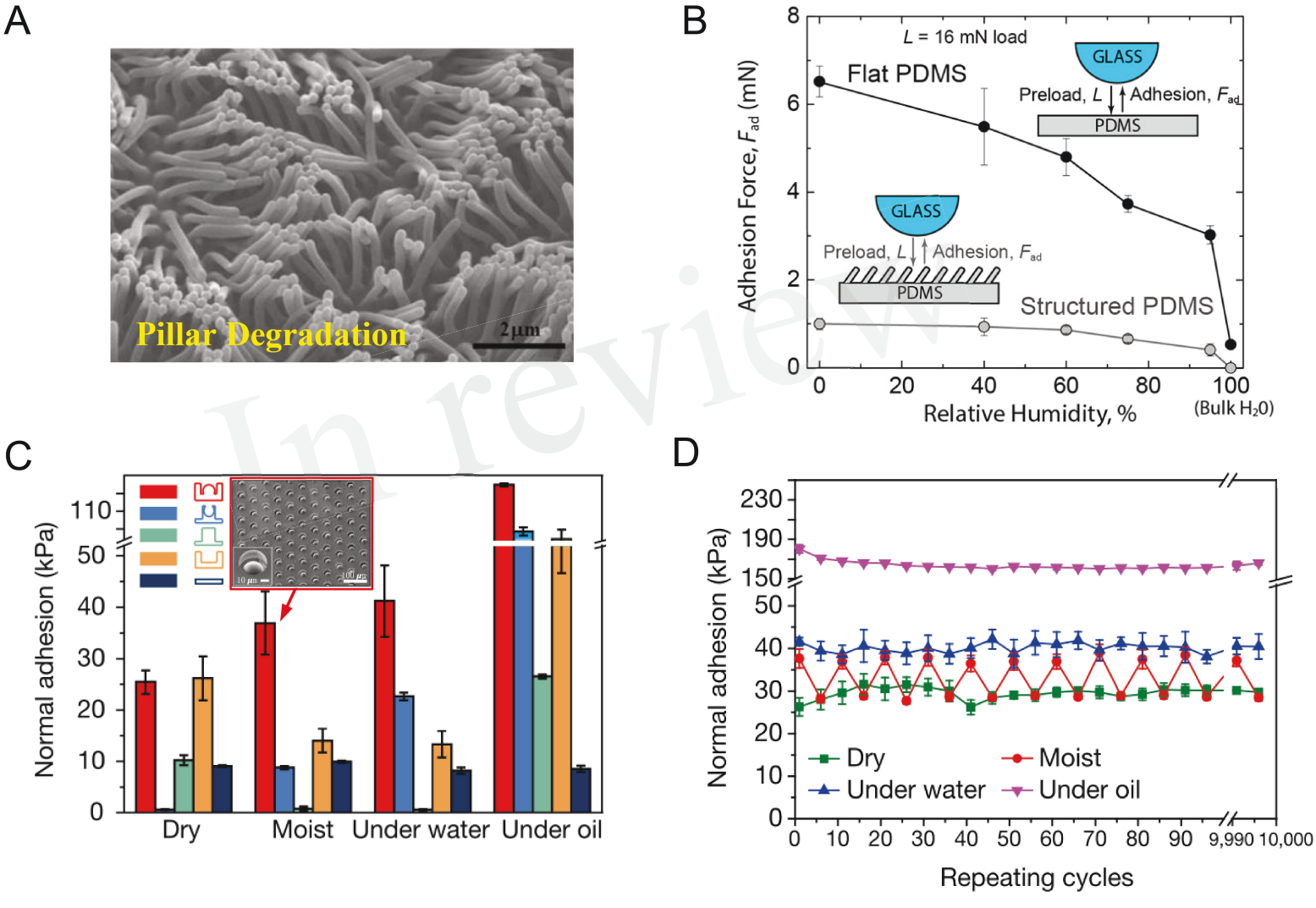

Figure 3.JPEG

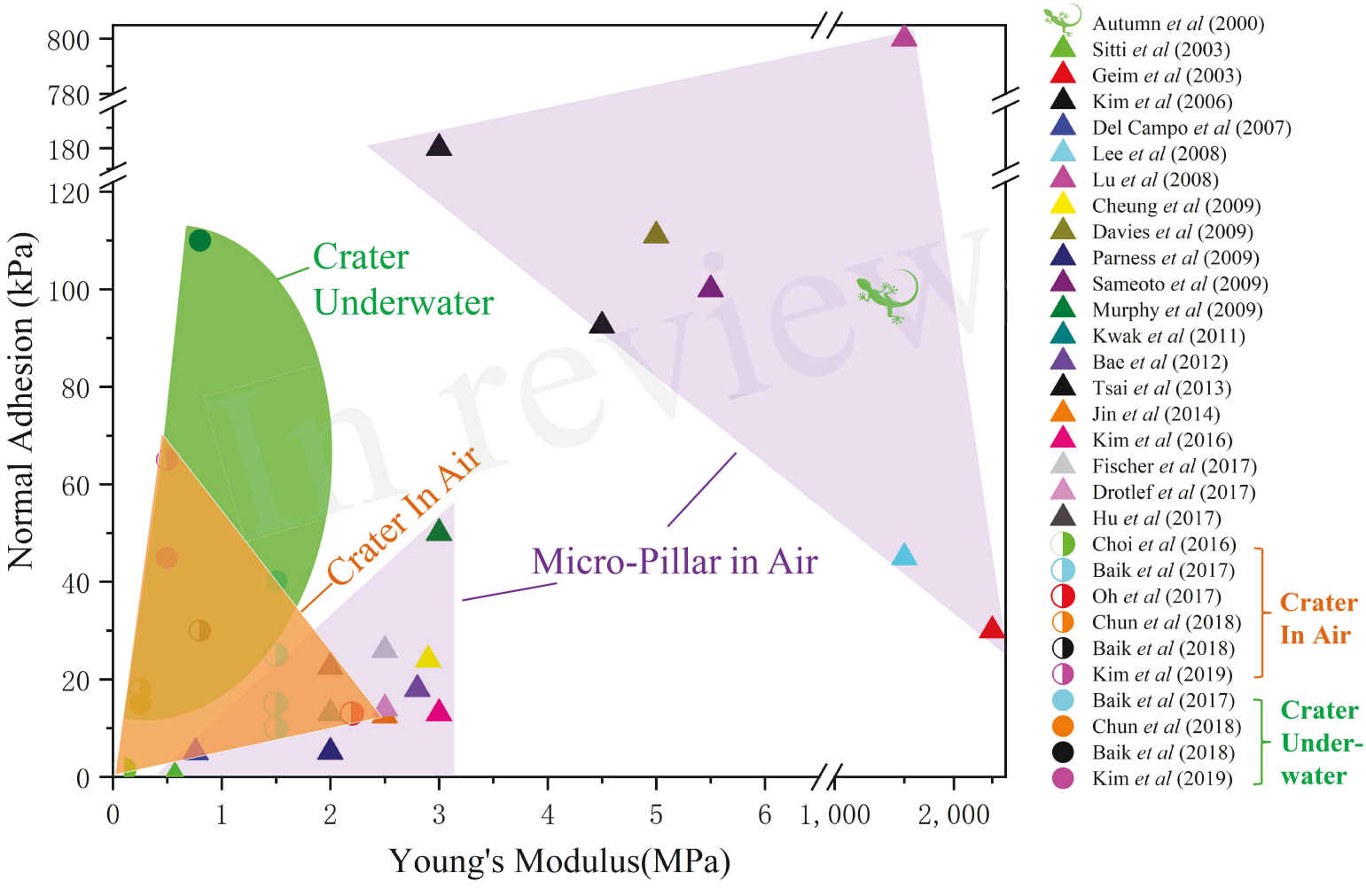

Figure 4.JPEG

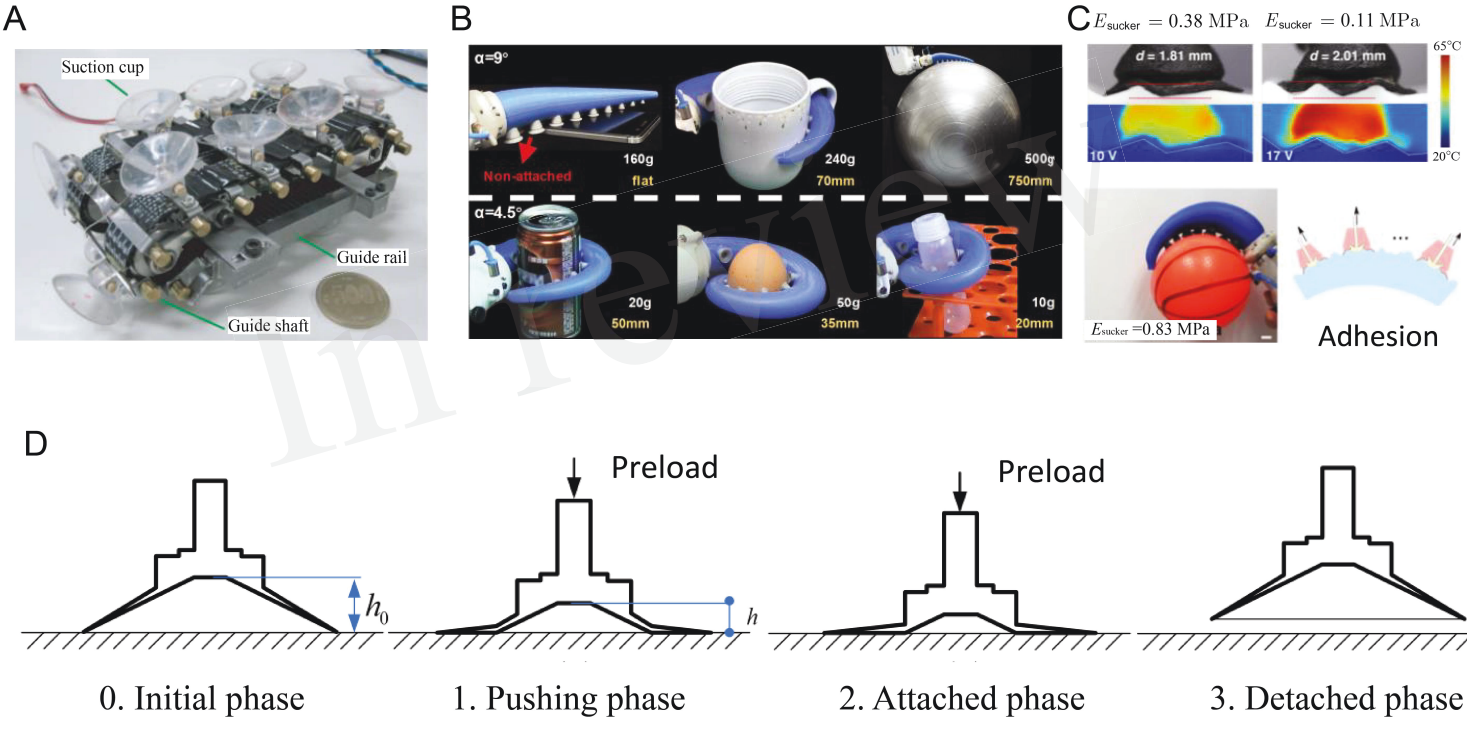

Figure 5.JPEG

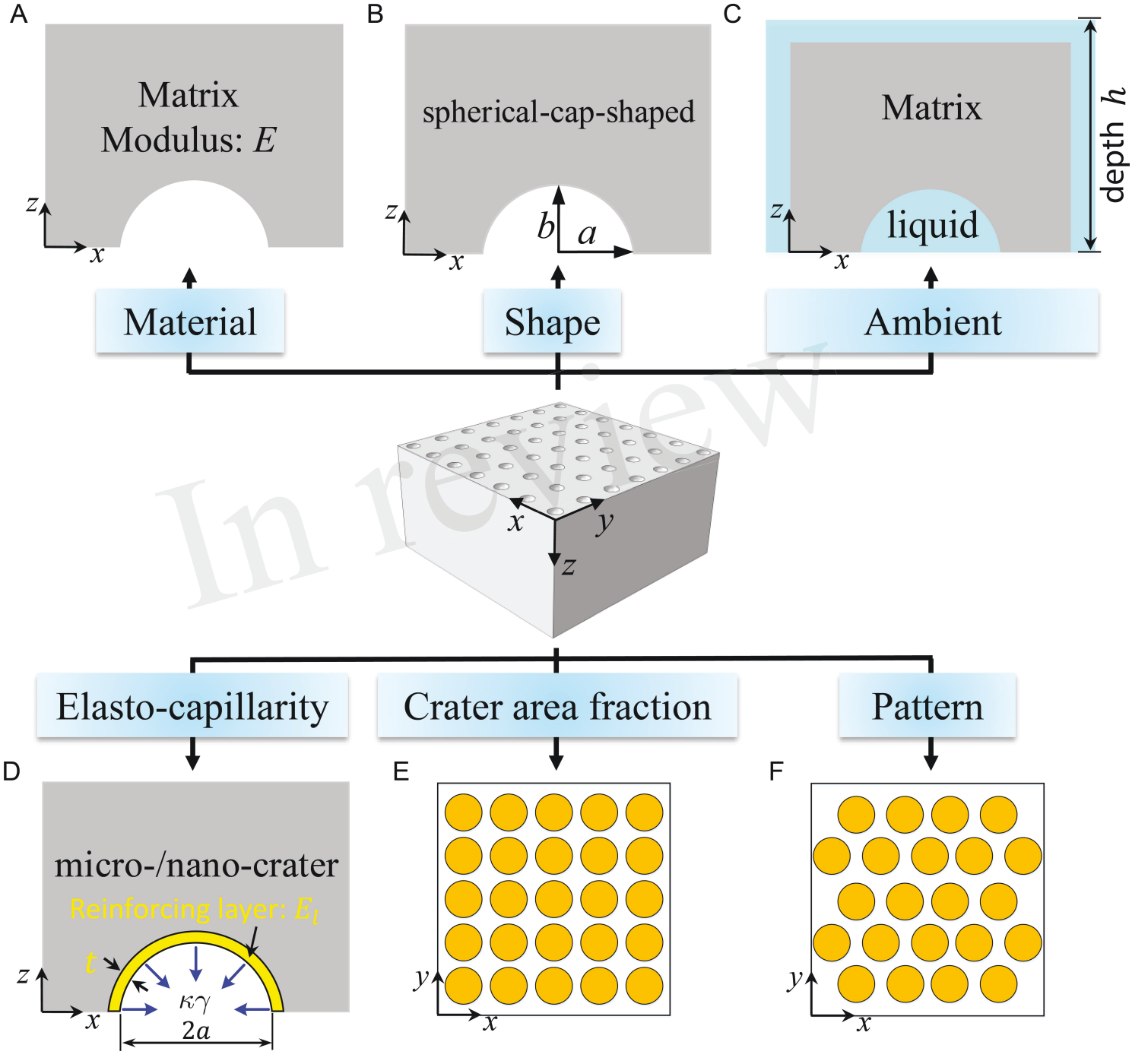

Figure 6.JPEG

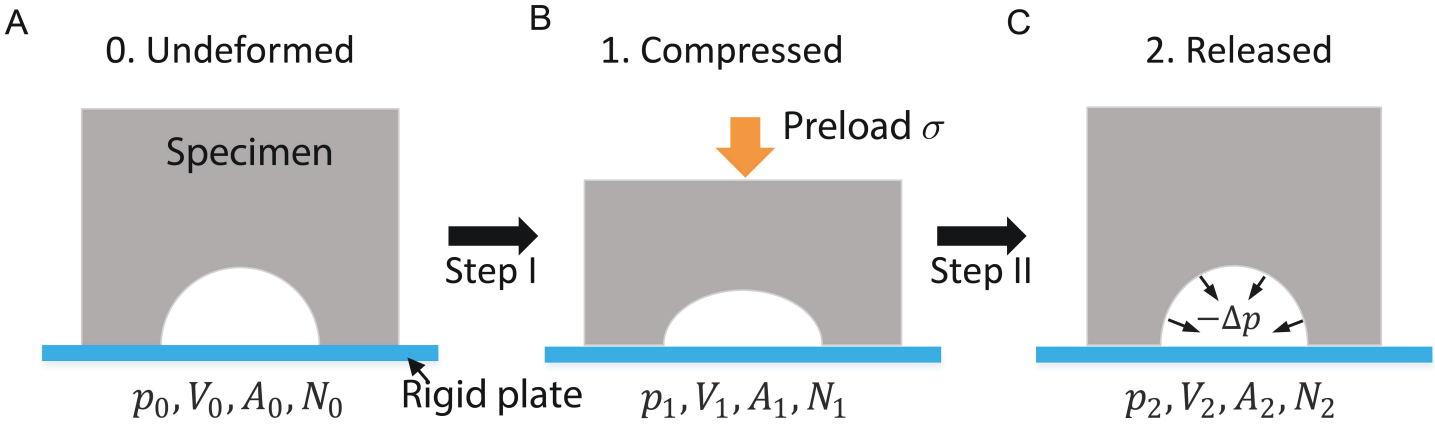

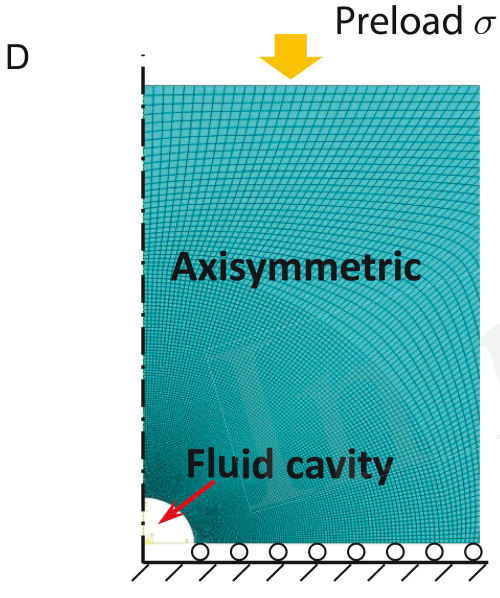

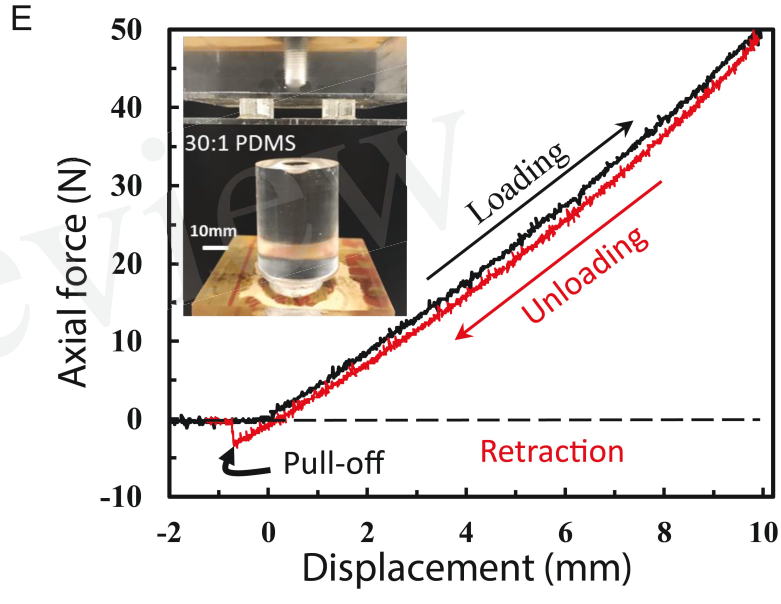

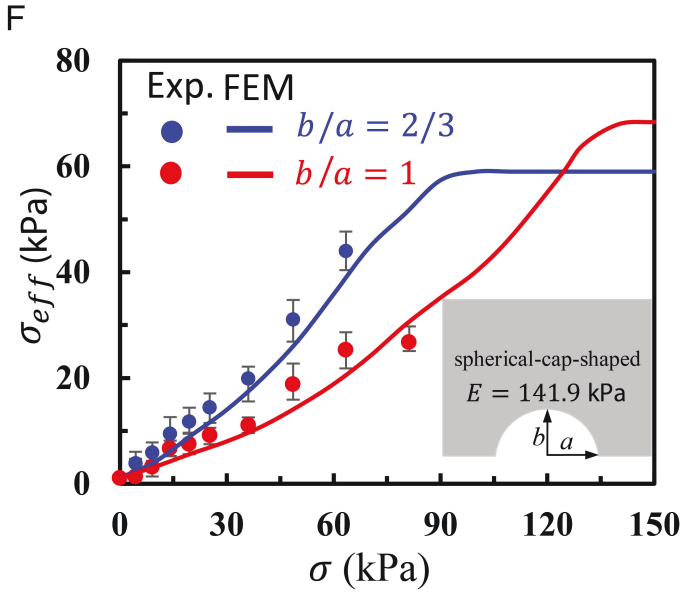

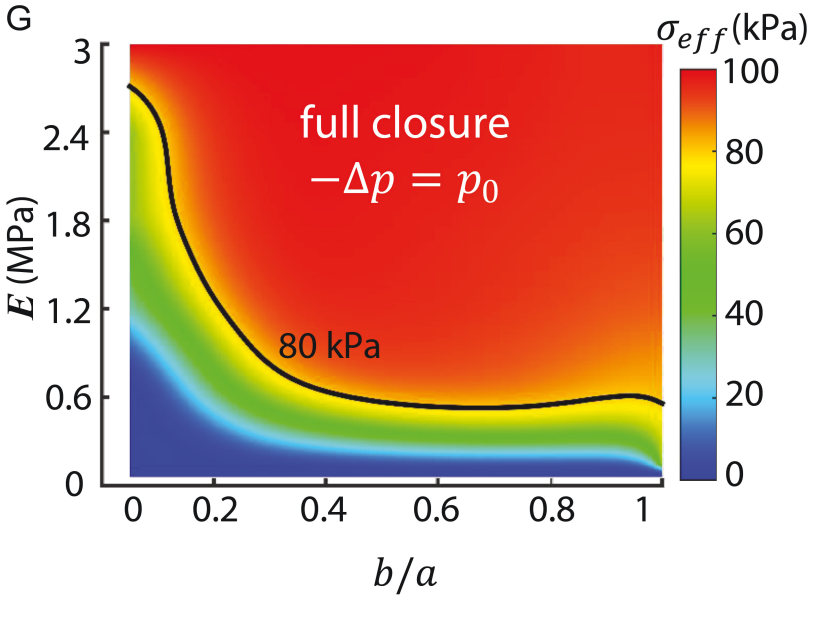

Figure 7.JPEG

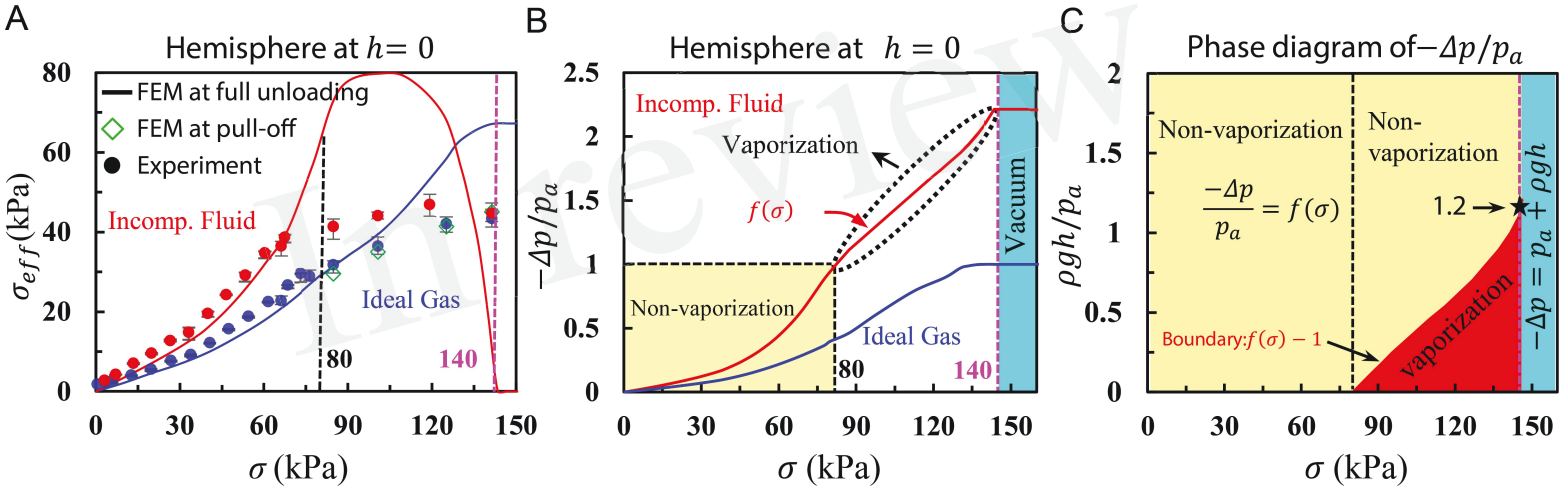

Figure 8.JPEG

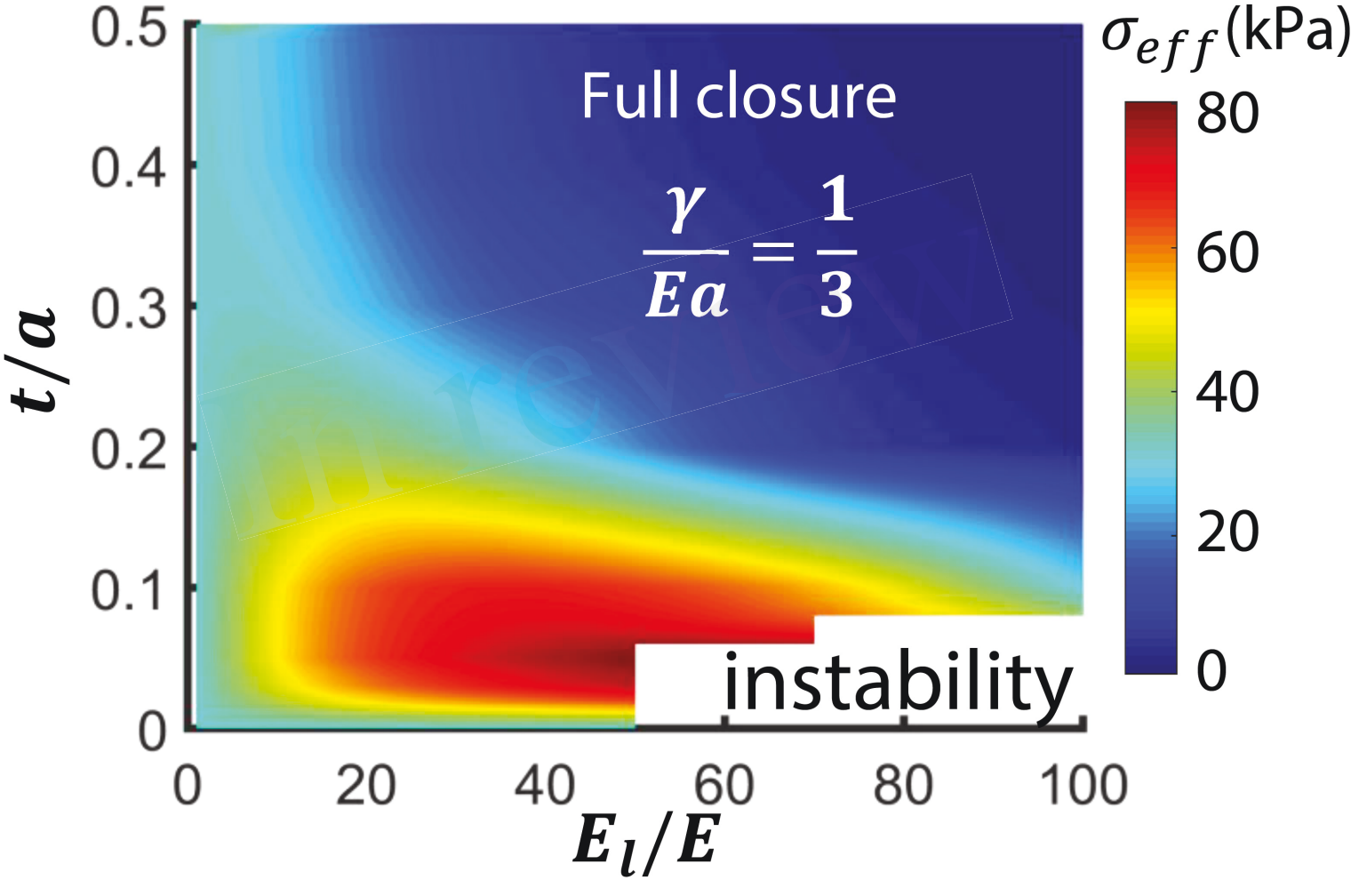

Figure 9.JPEG